THE JOURNAL OF BIOLOGICAL CHEMISTRY VOL. 290, NO. 11, pp. 7114–7129, March 13, 2015

Deficiency of the Chromatin Regulator Brpf1 Causes Abnormal Brain Development*[S]

Received for publication, December 24, 2014 Published, JBC Papers in Press, January 7, 2015, DOI 10.1074/jbc.M114.635250

Linya You[‡§], Jinfeng Zou[¶], Hong Zhao[‡], Nicholas R. Bertos[‡], Morag Park[‡§‖], Edwin Wang[¶], and Xiang-Jiao Yang[‡§‖**1]**

*From the [‡]Rosalind & Morris Goodman Cancer Research Center, [§]Department of Medicine, McGill University, Quebec H3A 1A3, the [¶]National Research Council Canada, Montreal, Quebec H4P 2R2, and the [‖]Department of Biochemistry, McGill University and **McGill University Health Center, Montreal, Quebec H3A 1A3, Canada*

Background: The chromatin regulator BRPF1 recognizes different epigenetic marks and activates multiple histone acetyltransferases, but little is known about its biological functions in mammals.
Results: Forebrain-specific inactivation of the mouse gene causes neocortical abnormalities and partial agenesis of the corpus callosum.
Conclusion: Mammalian BRPF1 is important for forebrain development.
Significance: This study links a unique chromatin regulator to mammalian brain development.

Epigenetic mechanisms are important in different neurological disorders, and one such mechanism is histone acetylation. The multivalent chromatin regulator BRPF1 (bromodomain- and plant homeodomain-linked (PHD) zinc finger-containing protein 1) recognizes different epigenetic marks and activates three histone acetyltransferases, so it is both a reader and a co-writer of the epigenetic language. The three histone acetyltransferases are MOZ, MORF, and HBO1, which are also known as lysine acetyltransferase 6A (KAT6A), KAT6B, and KAT7, respectively. The *MORF* gene is mutated in four neurodevelopmental disorders sharing the characteristic of intellectual disability and frequently displaying callosal agenesis. Here, we report that forebrain-specific inactivation of the mouse *Brpf1* gene caused early postnatal lethality, neocortical abnormalities, and partial callosal agenesis. With respect to the control, the mutant forebrain contained fewer Tbr2-positive intermediate neuronal progenitors and displayed aberrant neurogenesis. Molecularly, Brpf1 loss led to decreased transcription of multiple genes, such as *Robo3* and *Otx1*, important for neocortical development. Surprisingly, elevated expression of different *Hox* genes and various other transcription factors, such as Lhx4, Foxa1, Tbx5, and Twist1, was also observed. These results thus identify an important role of Brpf1 in regulating forebrain development and suggest that it acts as both an activator and a silencer of gene expression *in vivo*.

In eukaryotic cells, nuclear DNA is elegantly packaged with histones and other proteins into chromatin, which in turn controls gene activities according to spatiotemporal signaling cues (1–3). Such control is altered in human diseases and provides pathological epigenetic mechanisms. These mechanisms were initially recognized in leukemia and other cancers (4–6), but it is now becoming clear that such mechanisms are also crucial in neurological disorders (7–9). For epigenetic regulation, chromatin is subject to various modifications, one of which is histone acetylation. The acetyltransferase CREB-binding protein and its paralog p300 are altered in Rubinstein-Taybi syndrome, a genetic disease with the characteristic of intellectual disability and predisposition to brain and other tumors (10, 11). Histone deacetylases also regulate neurological processes. HDAC2 displays increased expression in patients with Alzheimer disease (12), and haploinsufficiency of HDAC4 causes brachydactyly mental retardation syndrome (13). The *HDAC10* gene is mutated in amyotrophic lateral sclerosis (14), and the mood-stabilizing drug valproic acid is a histone deacetylase inhibitor (15). These findings support the importance of histone acetylation modifiers in neurological diseases.

MOZ (monocytic leukemia zinc finger protein) is an acetyltransferase paralogous to MORF (MOZ-related factor) (16). MOZ was identified during analysis of acute myeloid leukemia (17), whereas MORF was uncovered based on sequence similarity to MOZ (18). Abnormal expression of mouse Moz contributes to metastasis of medulloblastoma (19), and inactivation of the mouse *Moz* gene partially phenocopies DiGeorge syndrome (20). Psychiatric illness is a late-occurring feature of this syndrome, and some patients are predisposed to schizophrenia. The *MORF* gene is mutated in four neurodevelopmental disorders as follows: Noonan syndrome-like disorder (21); Ohdo syndrome (22); genitopatellar syndrome (23, 24); and blepharophimosis-ptosis-epicanthus inversus syndrome (25). Intellectual disability is common to these disorders, and the patients often display callosal aplasia or hypoplasia (26). Related to the intellectual disability, mice with low Morf expression exhibit an abnormal cerebral cortex (27). No callosal abnormalities, however, have been reported for the mutant mice.

BRPF1 interacts with MOZ and MORF to stimulate their acetyltransferase activity, restrict the substrate specificity, and regulate related transcription (28, 29), suggesting that BRPF1

* This work was supported by grants from Canadian Institutes of Health Research, Natural Sciences and Engineering Research Council of Canada, and the Canadian Cancer Society (to X. J. Y.).
[S] This article contains supplemental Video S1 and Table S1.
[1] To whom correspondence should be addressed. Tel.: 514-398-5883; Fax: 514-398-6769; E-mail: xiang-jiao.yang@mcgill.ca.

may be an important modifier of neurological disorders resulting from aberrant MOZ and MORF. Moreover, BRPF1 interacts with and activates HBO1 (histone acetyltransferase bound to ORC1), which possesses a catalytic domain highly homologous to those of MOZ and MORF (30). Interestingly, genetic analysis of Chameau, the fly ortholog of HBO1, revealed an unexpected role in silencing *Hox* gene expression (31). In addition to association with histone acetyltransferases, BRPF1 possesses double plant homeodomain-linked (PHD) zinc fingers for interaction with histone H3 (30), a bromodomain with acetyl-lysine-recognizing ability (32) and a PWWP domain possessing specific affinity for methylated histone H3 (33, 34). Thus, BRPF1 is a multivalent chromatin regulator.

Biologically, mouse Brpf1 is essential for embryogenesis (35). Pathologically, the human *BRPF1* gene is recurrently mutated in sonic hedgehog-driven adult medulloblastoma (36). Moreover, related to the aforementioned possibility that BRPF1 functions as a modifier of neurological disorders resulting from aberrant MOZ and MORF, mouse Brpf1 is highly expressed in the forebrain and cerebellum (35), suggesting a role in brain development. To investigate this, we have specifically inactivated the mouse *Brpf1* gene in the forebrain. Here, we describe the resulting early postnatal lethality and characterize the developmental defects in the neocortex and corpus callosum. Strikingly, microarray-based gene expression analyses revealed dramatically elevated expression of multiple *Hox* genes and other transcription factors, thereby unveiling an unexpected role of Brpf1 in negative regulation of gene expression *in vivo*.

MATERIALS AND METHODS

Maintenance of Mouse Colonies and Use of Mice—Mouse strains were maintained in an established facility at McGill University, and all procedures about the use of mice were performed according to guidelines and protocols approved by the McGill Animal Use Committee. Heterozygous *Brpf1*$^{f/+}$ mice have been described recently (35). This conditional allele contains two LoxP sites for Cre-mediated excision to remove coding exons 4–6 of the *Brpf1* gene (35). Intercrosses generated *Brpf1*$^{f/f}$ homozygotes, which were then crossed with Emx1-Cre mice (Jax). Further intercross yielded forebrain-specific *Brpf1*$^{f/f}$;*Emx1-Cre* knock-out (or bKO) mice.

Behavioral Tests—Nest-building tests were performed as described (37). Between 4:00 and 5:00 pm, mice were transferred to individual testing cages with bedding but no environmental enrichment items. One nestlet cotton (3.0 g) was placed in each cage. The nests were assessed in the next morning on a 5-point scale as described (38). Digital cage photos were taken before and after the tests.

Hindlimb clasping tests were performed as reported (39). Mice were suspended by the base of the tail and videotaped for 14 s. Animals were assessed for hindlimb clasping score and duration. For the clasping score, the video was played back in half-time. The test period was divided into 2-s slots. An animal would receive a score of 1 point if it displayed any abnormal movement during the given time slot, thereby allowing for a maximum score of 7 points. An abnormal movement was defined as any dystonic movement of the hindlimbs, or a combination of hind- and forelimbs and trunk, during which the limbs were pulled into the body in a manner not observed in wild-type mice.

Nissl Stain—Tissue preparation was performed as described (40). Cryosections were prepared and air-dried before staining. Paraffin sections were dewaxed and rehydrated through a gradient series of ethanol. Cryosections or paraffin sections were stained in 0.1% cresyl violet solution (prepared with 0.3% glacial acetic acid and filtered) for 6–8 min, rinsed in distilled H_2O, dehydrated in a gradient of ethanol, cleared in xylene, and covered with glass coverslips for examination under a light microscope. Slides were also digitized with a Scanscope XT (Aperio) for further analysis.

Timm's Stain—This method stains vesicular zinc in the brain and was performed according to an on-line protocol (Nikki Sunnen, BCM 4/09). Wild-type and bKO mice were anesthetized at P8 with isoflurane and perfused transcardially with cold PBS and then with a buffered sulfide solution containing 1.2% Na_2S. Brains were removed and immersed in the perfusion solution for 1 h. After rinsing with distilled H_2O, the brains were fixed in neutral buffered formalin (Sigma, HT501128) for 24 h and post-fixed in 3% glutaraldehyde in 30% dextrose solution for 1.5 h. Samples were embedded in paraffin and serially sectioned sagittally at 5 μm. Dewaxed and rehydrated slides were stained in a preheated (26 °C) Timm's stain solution (30% gum arabic, 1.7% hydroquinone and 0.085% silver nitrate in the citrate buffer) for 45 min in the dark at room temperature and then for at least 20 min at 60 °C. Slides were counterstained in 0.1% cresyl violet.

Myelin Staining—The Black Gold II myelin staining kit was used according to the manufacturer's instructions (Millipore, AG105). Wild-type and bKO mice at P13 were anesthetized with isoflurane and perfused transcardially with cold PBS and then with 4% paraformaldehyde in PBS. The brains were removed and immersed in 4% paraformaldehyde overnight at 4 °C. 40 μm of coronal cryosections were used.

Golgi-Cox Staining—After anesthesia, mice were perfused transcardially with cold PBS. Golgi-Cox impregnation was performed with the FD Rapid Golgi-Stain kit (FD NeuroTechnologies, PK401A) according to the manufacturer's instructions. For this, 180-μm coronal slices were prepared on a Vibrotome (Bio-Rad/EM Corp., Micro-Cut H1200). Black and white photographs were taken under a bright field on an Axio Observer Z1 microscope controlled by the Zen software package (Zeiss).

Immunofluorescence Microscopy—This was performed as described previously (40, 41). The following antibodies were used: rabbit anti-Cux1 (1:200) (42); rat anti-Ctip2 (Abcam, ab18465, 1:400); rabbit anti-Tbr2/Eomes (Abcam, ab23345, 1:400); goat anti-Sox2 (R&D Systems, AF2018, 1:200); mouse anti-phospho-Ser-10 histone H3 (USBiological Life Sciences, H5110-13K, 1:100); rabbit anti-cleaved caspase 3 (Asp-175) (Cell Signaling, 9661, 1:200); Alexa Fluor 568-conjugated goat anti-rabbit IgG (Invitrogen, A11011, 1:500); Alexa Fluor 568-linked goat anti-mouse IgG (Invitrogen, A11031, 1:500); Alexa Fluor 488-labeled goat anti-rat IgG (Invitrogen, A11006, 1:500), and Cy3-conjugated anti-goat IgG (Molecular Probes, 1:500) antibodies.

Measurement of Cortical Layer Thickness—After DAPI staining, fluorescent images were taken, and cortical layer thickness

TABLE 1
RT-PCR primers

Target gene	Primer sequence		Primer position	GenBank™ accession no.
	Upstream	Downstream		
Brpf1	CAGTAAGATCACCAACCGCC	GAGGAAAGGGGTCAGCTGCA	1711–2050	NM_030178.1
Emx1	GGGCTCCTCCTCGCTGCAAC	TCTTGATTGTTCCCCTAGTC	330–800	NM_010131
Tbr1	TTTTTGAGTTTTAACATTTC	GAAGCGGGCCTTGGCGTAGT	960–1590	NM_009322
Pax6	GGCGACTCCAGAAGTTGTAA	TTGCAGCTTCCGCTTCAGCT	560–960	NM_001244198
Bdnf	TTCCACCAGGTGAGAAGAGT	GTCGGAGTGGCGCCGAACCC	641–1060	NM_007540.4
Reelin	GCGGGCTCTCGTCCTGGCCG	GCAATCCAGACAAAGCTGAG	321–740	NM_011261.2
Fezf2	AGACACAAAATTATCCATAC	CTGCAAAAACCTTTGCCGCA	1280–1600	NM_080433.3
Rorβ	CACCCTGTGGCCACGACATC	GCTGCTCCTGCAGCCTTTGC	480–960	NM_001043354.2
Nr2f1	GAAGTGCCTCAAAGTGGGCA	TCCTGAAAGATGCGGATGTG	721–1200	BC108408
Gapdh	TGATGACATCAAGAAGGTGGTGAA	TCTTACTCCTTGGAGGCCATGT	814–1059	XM_001476707.3

was measured with the Zen software package (Zeiss). The neocortex above the hippocampus was selected for quantification. For E15.5 neocortex, the total thickness was divided into ventricular zone/subventricular zone, intermediate zone, and cortical plate. For quantification, three brains per genotype and three sections per brain were measured. Neonate cortex was considered to include the subventricular zone, intermediate zone, and layers I–VI; for quantification, three brains per genotype and 4–5 sections per brain were measured.

After double immunolabeling with anti-Ctip2 and -Cux1 antibodies, images were taken with the Zen software package (Zeiss) to determine thickness of the $Cux1^+$ or $Ctip2^+$ layer, signal intensity of the $Cux1^+$ layer, and cell density in the $Ctip2^+$ layer. Three brains per genotype and three sections per brain were used for quantification.

Cortical Neuronal Migration Analysis—After intraperitoneal injection with 50 μg of BrdU/g body weight at E12.5, E14.5, and E16.5, pregnant mice were sacrificed at P0 to retrieve neonate brains for fixation and subsequent preparation of 5-μm paraffin sections. For immunostaining, the sections were dewaxed, rehydrated, and exposed to 2 N HCl at 37 °C for 30 min before antigen retrieval by boiling in 10 mM sodium citrate at pH 6.0 for 20 min. Sections were then incubated in the blocking solution (2% BSA and 0.2% Triton X-100 in PBS) at room temperature for 1 h before incubation with a rat anti-BrdU antibody (Abcam, AB6326, 1:100) in the blocking solution at 4 °C overnight. Biotin-SP-conjugated AffiniPure donkey anti-rat IgG(H+L) (Jackson ImmunoResearch, 712-065-153, 1:200) was used as a secondary antibody. The signal was developed with the Vector ABC and DAB substrate kits (Vector Laboratories, PK-4001 and SK-4100). Stained sections were archived on a Scanscope XT (Aperio) with a 20× objective. The developing neocortex above the hippocampus was used for quantification. For each cortex, the total thickness extending from molecular layer to the intermediate zone was divided into 10 bins with Photoshop (Adobe), and the cell number of darkly stained and lightly stained $BrdU^+$ cells was counted manually and assigned to each bin to generate histograms of the number of labeled cells against bin. The genotypes were intentionally ignored to avoid bias. For each BrdU labeling time point, two pairs of littermates and four matched sections per pair were used for quantification.

Cell Cycle Analysis—Pregnant mice were intraperitoneally injected at E15.5 with 50 μg of BrdU/g body weight, and fetal brains were recovered 1 h later. Paraffin sections were prepared for immunostaining with anti-Ki67 and -BrdU antibodies. For antigen retrieval, the sections were boiled in 10 mM sodium citrate at pH 6.0 for 20 min, blocked, and incubated simultaneously with rat anti-BrdU antibody (Abcam, AB6326, 1:100) and mouse anti-Ki67 antibody (Pharmingen, 556003, 1:400) at 4 °C overnight. Alexa Fluor 488-conjugated goat anti-rat IgG (Invitrogen, A11006, 1:500) and Alexa Fluor 568-conjugated goat anti-mouse IgG (Invitrogen, A11031, 1:500) were used as the secondary antibodies. After counterstaining with DAPI, fluorescent images were taken on an Axio Observer Z1 fluorescence microscope (Zeiss) controlled by the Zen software package (Zeiss). The subventricular zone (SVZ)[2] above the hippocampus was boxed using the Zen software package (Zeiss) for manual counting of $BrdU^+$ and/or $Ki67^+$ cells; during counting, the genotypes were intentionally ignored to avoid bias. The SVZ region was chosen for quantification based on published reports (43, 44), and the SVZ precursor cells were identified as those set apart from the dense layer of $BrdU^+$ cells in the ventricular zone as described (45). The quantification was performed on two pairs of littermates and 4–5 matched sections per animal.

RT-PCR—This was performed as described (40), with primers listed in Table 1.

Microarray Analysis—Total RNA was isolated from three pairs of wild-type and mutant dorsal caudal cortices at P4 using the miRNeasy mini kit (Qiagen). The yield was measured on a Nanodrop 2000 spectophotometer (Thermo Scientific), and the integrity was assessed with an RNA Pico chip on an Agilent 2100 Bioanalyzer (Agilent Technologies). 500 ng of total RNA was subjected to a single round of amplification with the Amino Allyl MessageAmp™ II amplified antisense RNA kit (Ambion/Invitrogen, AM1753) according to the manufacturer's instructions. The amplified product was labeled with a CyDye Post-Labeling Reactive Dye Pack (GE Healthcare). Cy3-labeled and Cy5-labeled aRNA probes (825 ng each) were co-hybridized to Agilent SurePrint G3 Mouse GE 8 × 60K microarray (Agilent Technologies, G4852). Microarray slides were washed according to the manufacturer's instructions and scanned on an Agilent dual-laser scanner. Feature extraction was performed with Agilent Feature Extraction software (version 9.5.3.1).

The Limma package was used to normalize and determine the modulated genes from the original microarray data (46). Signal background correction was carried out by use of the normexp method and offset = 50 as suggested by the Limma

[2] The abbreviations used are: SVZ, subventricular zone; qPCR, quantitative PCR.

TABLE 2
RT-qPCR primers

Target gene	Primer sequence		Primer position	GenBank™ accession no.
	Upstream	Downstream		
Brpf1	CAGTAAGATCACCAACCGCC	GAGGAAAGGGGTCAGCTGCA	1711–2050	NM_030178.1
Moz	ATGGTAAAACTCGCTAACCCG	CGTCCCGTCTTTGACGCTC	1–177	NM_001081149
Morf	AGAAGAAAAGGGGTCGTAAACG	GTGGGAATGCTTTCCTCAGAA	2474–2668	NM_017479
Hbo1	ATGCCGCGAAGGAAGAGAAAT	TCTTGGGAACTCTGGCTTAGC	1–164	NP_808287
Hoxc6	AATTCCACCGCCTATGATCCA	ACATTCTCCTGTGGCGAATAAAA	79–182	NM_010465
Hoxb13	GGGGTCGGAATCTAGTCTCCC	CCTCCAAAGTAGCCATAAGGCA	68–257	NM_008267
Hoxc4	CTACCCTGAGCGTCAGTATAGC	CGCAGAGCGACTGTGATTTCT	183–295	X69019
Hoxb5	CCTTCTCGGGGCGTTATCC	CCTGAAGCGGGGTTCCTTG	23–258	M26283.1
Hoxd8	CTTCGTGAACCCGCTGTACTC	GACAGTCGTAGTAAGTGGGATTG	12–118	NM_008276
Hoxc10	ATGACATGCCCTCGCAATGTA	CCCCGCAGTTGAAGTCACTC	1–127	NM_010462
Lhx4	GGCTGCAACCAACATATCCTG	CATTTTGTGCCAAAGCGTTTGA	94–266	NM_010712
Pou4f1	CGCGCAGCGTGAGAAAATG	CGGGGTTGTACGGCAAAAT	1020–1142	NM_011143
Foxa1	ATGAGAGCAACGACTGGAACA	TCATGGAGTTCATAGAGCCCA	29–133	NM_008259
Tbx5	ATGGCCGATACAGATGAGGG	TTCGTGGAACTTCAGCCACAG	1–207	NM_011537
Twist1	GGACAAGCTGAGCAAGATTCA	CGGAGAAGGCGTAGCTGAG	432–577	NP_035788
En2	GCTGGCACTACCGAAGGAG	ACCGTGAAGTGATAGCGTCTT	292–468	NM_010134
Hmx1	GTCCTGACACAAGCGACCG	GCTTCAGATCGAAAGTGGACTC	365–640	NM_010445
Pitx2	GCAGCCGTTGAATGTCTCTTC	GTCCGTGAACTCGACCTTTTT	58–117	NM_011098
Pax1	CCGCCTACGAATCGTGGAG	CCCGCAGTTGCCTACTGATG	330–397	NM_008780
Onecut1	GGCAACGTGAGCGGTAGTTT	TTGCTGGGAGTTGTGAATGCT	427–585	NM_008262
Onecut2	CTCAGCCCCAATTTCGACG	GTAAGCCATTGAGGTGAGACATC	775–889	NM_194268
Nkx2–3	AAGGGACGCAGTTTTCCGATG	GCAGCAGCTAGTGAGTTCAAATA	149–233	NM_008699
Spag61	AACCCCGATGAGAAACTGAAG	AAATCTCTGCCTCCACAACC	705–804	BC061194
Robo3	AGATGAACTTGTTCGCGGACT	GGAAGCAGACTAGGGTTGAGC	32–137	NM_001164767
Ostn	CTGGAGATTGGCAAGTACACAC	CGCAGGAGCTTAGCCGAAA	9–182	NM_198112
Cmtm2a	TCAGGAAGACCACCAGTACAG	CACACGGGCTCCATCTTTT	347–450	AK006874
Cxcl15	CAAGGCTGGTCCATGCTCC	TGCTATCACTTCCTTTCTGTTGC	10–192	NM_011339
Dkk1	CTCATCAATTCCAACGCGATCA	GCCCTCATAGAGAACTCCCG	109–213	NM_010051
Hif3a	GAAGTTCACATACTGCGACGA	GTCCAAAGCGTGGATGTATTCAT	741–840	NP_058564
Msx3	ACCCTCCGCAAACACAAAAC	CGCTCCGCAATGGATAAGTAT	238–350	NM_010836
Wt1	GAGAGCCAGCCTACCATCC	GGGTCCTCGTGTTTGAAGGAA	619–746	NM_144783
Rhox9	TCCACAGGCTGGGAACTATCT	AAGCTGGGGAAGCGATTCTC	423–533	NM_023894
Prok1	CCTGCTGCGCTATCAGTCTG	GGCGTTTCCTCAAGAAGGGG	107–220	NM_001044382
Sod2	CAGACCTGCCTTACGACTATGG	CTCGGTGGCGTTGAGATTGTT	86–198	NM_013671
Arfip1	CTGCTGGCTAAAAATGGAGAGA	GCGGTACGCATCATATTCAACT	667–813	NM_001081093
Als2cr12	TTCATCTACTGTACCTGCTGTGA	ACTGGCTTAAACTTCCCCGTG	16–119	NM_175370
Commd10	GCTTGGTCGGCTATGGGTC	GTTAAGCTGCCATCCCACTGT	334–426	NM_178377
Unknown	ATCACTTGCACCCCGGTTTC	AGTACCCTTATAGGCATCCCG	85–276	NM_207248
Unknown	AGCATCCTCCTTCCACCTGA	TGCTTGTGGGCAGAAGAGAA	583–688	AK143833
Rps19	CAGCAGGAGTTCGTCAGAGC	CACCCATTCGGGGACTTTCA	31–102	NM_023133
Rpl13	AGCCGGAATGGCATGATACTG	TATCTCACTGTAGGGCACCTC	10–197	NM_016738
Rpl26	ACTTCTGACCGAAGCAAGAAC	CCGAATGGGCATAGACCGAA	22–150	NM_009080
Rpl41	CATCTTCCTTGAGACTCCTGC	CATCCCTCACTTCTGCTCC	16–167	NM_018860
Rpl38	GAAGTTCAAGGTTCGCTGC	TTTAATAGTCACACGCAGAGGG	211–355	NM_001048057
Rps26	TCATTCGGAACATTGTAGAAGCC	ACAGCTCACGCAATAATGCAG	119–231	NM_013765
Rps29	GTCTGATCCGCAAATACGGG	AGCCTATGTCCTTCGCGTACT	86–154	NM_009093
Rn18S	CACGGACAGGATTGACAGATT	GCCAGAGTCTCGTTCGTTATC	1277–1396	NR_003278.3
Gapdh	TGATGACATCAAGAAGGTGGTGAA	TCTTACTCCTTGGAGGCCATGT	814–1059	XM_001476707.3

package. To determine the modulated genes between a mutant and its wild type, we applied two-channel normalization. Within-array normalization was carried out with the Loess method, although between-array normalization was performed by a quantile method (46). Empirical Bayes statistics were applied to determine the differential expression of the genes. Original microarray data and normalized datasets have been deposited in the GEO database under the accession number GSE63909. The resulting gene list is presented in supplemental Table S1.

RT-qPCR—Total RNA was isolated from three pairs of wild type and mutant dorsal caudal cortices at P12 with the miRNeasy mini kit (Qiagen). cDNA was synthesized using the Quantitect reverse transcription kit (Qiagen). Real time qPCR was conducted with the Green-2-Go qPCR Mastermix (Bio-Basic) on Realplex2 (Eppendorf). Primers were taken either from PrimerBank or designed on the web-based qPCR primer designer (IDT Biotechnology). Primers (Table 2) were synthesized by IDT Biotechnology.

Immunoblotting—Three pairs of P12 control and bKO dorsal caudal cortices of the forebrain were dissected and homogenized in 500 μl of RIPA buffer (150 mM NaCl, 50 mM Tris-HCl, pH 8.0, 1% Triton X-100, 0.5% sodium deoxycholate, 0.1% SDS, 1 μg/ml pepstatin, 2 μg/ml aprotinin, 5 μg/ml leupeptin, and 1 mM PMSF) and sonicated. The lysate was then rotated at 4 °C for 1 h and centrifuged at 16,000 $\times$ *g* and 4 °C for 20 min. The supernatant protein concentration was determined with a protein assay reagent (Bio-Rad, 500-0006), and protein lysates (40 μg/lane) were separated by SDS-PAGE for transfer onto nitrocellulose membranes (Pall Corp., P/N66485). After blocking, membranes were incubated overnight at 4 °C with goat anti-Hoxc4 (Santa Cruz Biotechnology, sc-49986, 1:200) or rabbit anti-histone H3 (Abcam, ab1791, 1:5000). Blots were washed extensively in PBST and incubated with horseradish peroxidase-conjugated donkey anti-rabbit (GE Healthcare, NA934V, 1:5000) or HRP-linked donkey anti-goat secondary antibody (Jackson ImmunoResearch, 705-035-147, 1:5000). Blots were developed with the enhanced chemiluminescence substrates (FroggaBio, 16024).

Statistical Analysis—Log-rank tests (for survival curve) and Student's tests were carried out with Prism 5 (GraphPad).

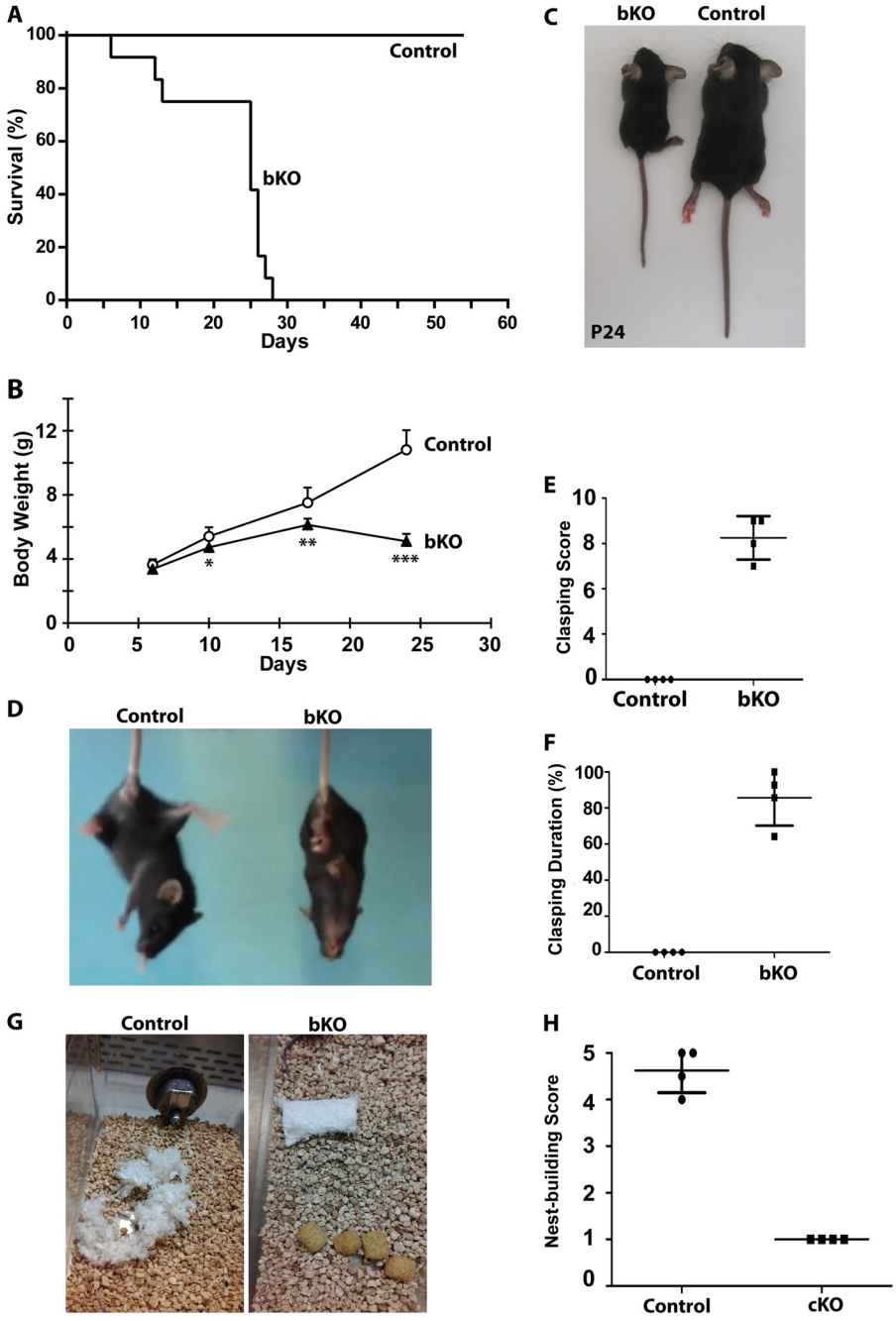

FIGURE 1. **Brpf1 inactivation causes postnatal lethality and abnormal behaviors.** *A,* survival curve of control and bKO mice. The increased mortality of the bKO mice is statistically significant: $p < 0.05$ ($n = 12$ mice for each group). *B,* starting from P10, the bKO mice failed to thrive. Data are shown as mean ± S.D. $n = 11$ mice for the wild-type group and $n = 6$ for the mutant group; *, $p < 0.05$ for P10; **, $p < 0.01$ for P17; and ***, $p < 0.001$ for P24. *C,* representative photo of bKO and control mice at P24. *D,* representative picture of the hindlimb-clasping test. The bKO mouse (*right panel*) displayed a characteristic full body clasping phenotype compared with the control mouse (*left panel*). *E* and *F,* four pairs of control and bKO mice were observed in a 14-s test procedure to monitor the clasping phenotype at P24. Mice were analyzed for clasping score (*E*) and duration (*F*). *G,* representative pictures of nest-building skills. The control mouse built a perfect nest (*left panel*), whereas the mutant left the cotton pad untouched (*right panel*). *H,* nest-building scores were evaluated for four pairs of control and bKO mice at P24.

RESULTS

Forebrain-specific Loss of Brpf1 Causes Early Lethality and Behavioral Abnormalities—To determine the function of Brpf1 in the mouse forebrain, we mated *Brpf1*$^{f/f}$ mice (35) with the *Emx1-Cre* strain, in which the Cre recombinase is specifically expressed in the neocortex and hippocampus starting as early as E10.5 (47). The resulting *Brpf1*$^{f/+}$;*Emx1-Cre* mice appeared normal, and further crosses yielded *Brpf1*$^{f/f}$;*Emx1-Cre* knockout (or bKO) mice. The pups were born at a ratio slightly lower than the expected Mendelian ratio (data not shown), suggesting partial prenatal lethality. After birth, a majority of the viable bKO pups died prior to weaning around postnatal day (P) 21, with a minority surviving afterward (Fig. 1*A*). The mutant pups did not display obvious abnormalities at birth, and the growth appeared normal at P5. However, at P10, they were significantly smaller than their control littermates (Fig. 1*B*). Those mutant

pups that survived after weaning were easily identifiable by their smaller size (Fig. 1*C*). They also consumed much less food than their control littermates (data not shown). Thus, forebrain-specific deletion of the *Brpf1* gene resulted in early postnatal lethality and growth retardation.

We then conducted behavioral tests with those mutant mice that survived after weaning. Hindlimb-clasping tests are often used as an indicator for motor and coordination skills (48). The bKO but not control mice displayed a characteristic full-body clasping phenotype (Fig. 1*D* and supplemental video S1). Semi-quantitative analysis of the clasping behavior was also carried out. For this, four control and four bKO mice were observed in a 14-s test procedure to monitor the clasping phenotype. Mice were scored for clasping severity and duration. The results revealed that bKO mice displayed a much higher tendency of hindlimb clasping (Fig. 1, *E* and *F*), indicating problematic motor coordination and neurological defects. We also assessed nest-building skills, which are learned by pups watching the mother and other cage mates and thus indicate learning ability and motor usage (37). Control mice consistently tore cotton pads provided in the cage and built perfect nests within the given time window (Fig. 1*G*, *left panel*). By contrast, mutant mice were unable to do so and left the cotton pad untouched (Fig. 1*G*, *right panel*). Semi-quantitative scoring revealed defective nest-building skills in the mutant (Fig. 1*H*). One rare mutant mouse survived to 45 days after birth and was old enough for marble-burying tests, which are often used to indicate repetitive, compulsive behaviors (49). Although the control littermate completely or partially buried 10 of the 12 marbles provided, the mutant left all 12 untouched (data not shown). Together, these results indicate that *Brpf1* inactivation in the forebrain caused behavioral and neurological defects.

Brpf1 Deficiency Alters Neocortical Development—We then investigated abnormalities at the tissue level. Compared with that of the control littermates, the bKO brain was slightly smaller (Fig. 2*A*, *left panel*), although the size remained proportional to the body size (Fig. 2*A*, *right panel*). The rostral-caudal length of the neocortex was shorter in the bKO brain (Fig. 2*B*, marked by *green arrowheads*). Acquired late during evolution, the neocortex is a mammal-specific forebrain structure comprising a uniform laminar structure that has been traditionally divided into layers I–VI (50). We thus systematically examined tissue histology by performing Nissl staining of serial sagittal and coronal sections of the control and mutant brains. Shown in Fig. 2*C* are two representative images from these sections. Compared with the control, the mutant neocortex was thinner and showed differences in lamination (Fig. 2*C*). By contrast, the cerebellum appeared normal (Fig. 2*D*). These results are in agreement with the fact that the Emx1-Cre strain expresses the Cre recombinase from the endogenous Emx1 locus to drive excision in the forebrain but not the mid- or hindbrain (47, 51).

Starting before birth, the cortical plate of the mouse brain gradually develops to form the laminated neocortex (50, 52). Immediately after birth, the cortical plate of the mutant brain was also thinner than that in the wild type (Fig. 2*E*), as confirmed by DAPI staining and quantification (Fig. 2, *F* and *G*). Moreover, the defect remained evident at E15.5 (Fig. 2, *H* and *I*). E15.5 is a mid-corticogenesis stage when lower layer neurons have differentiated and are migrating to the cortical plate (53). The thinner cortical plate at E15.5 (Fig. 2, *H* and *I*) is consistent with the thinner layers V–VI at P0 (Fig. 2, *F* and *G*).

To characterize the lamination defects further, we performed Timm's stain on serial sagittal brain sections. As reported (54), the wild-type neocortex contained two darkly stained bands (Fig. 3*A*). In the mutant neocortex, the superficial band was present, but the inner band was missing (Fig. 3*A*). These results provide further support for defective lamination in the mutant neocortex.

Golgi-Cox staining has been widely used to reveal axonal and dendritic structures of neurons (55), so we next utilized this technique to examine how *Brpf1* inactivation may affect cortical neuron distribution and structures. As shown in Fig. 3*B*, neurons in the bKO neocortex were less organized. Moreover, the neuron density was lower, and dendritic trees were less sophisticated in the mutant neocortex (Fig. 3*C*).

Taken together, results from the above morphological and histological analyses (Figs. 2 and 3) indicate that specific inactivation of the *Brpf1* gene in the forebrain led to formation of abnormal neocortical organization. Brpf1 is thus required for neocortical development.

Brpf1 Regulates Cortical Neurogenesis—To gain molecular insights into the lamination defects, we analyzed expression of markers for different layers of the neocortex. For this, indirect immunofluorescence microscopy was performed with antibodies against Cux1 and Ctip2, well known markers of layers II/III/IV and V/VI of the neocortex, respectively (56, 57). At P0, Cux1 expression was slightly altered in the bKO neocortex (Fig. 4*A*). Compared with the wild type, a narrower $Ctip2^+$ layer was observed in the mutant brain (Fig. 4, *B* and *C*). These results provide support for the lamination defects at the molecular level.

Through an inside-out mechanism, cortical neural precursors produce neurons of layers VI–V from E11.5 to E15.5 and then generate those in layers II–IV from E14.5 to E17.0 (50, 52). Thus, we used neuronal birthdating assays, as described previously (58, 59), to investigate whether neurons are produced at the correct time and then migrate properly to different cortical layers. For this, BrdU was injected into pregnant dams at E12.5, E14.5, and E16.5, and the dams were sacrificed at P0 to recover neonate brains for immunohistochemical analyses with anti-BrdU monoclonal antibody. The staining patterns observed in control neonate brain sections (Fig. 5) were very similar to what was reported by others (58, 59). As in the control, E12.5 labeling revealed a peak of $BrdU^+$ neurons in cortical layers V–VI, corresponding to bins 5–8, in the mutant (Fig. 5*A*). There was only a slight decrease in the number of densely labeled neurons in bin 8 of the mutant (Fig. 5*B*), indicating that a majority of neurons born at E12.5 migrate correctly to different neocortical layers. E14.5 labeling uncovered a significant decline of mutant $BrdU^+$ neurons in bins 2–4, corresponding to cortical layers II–IV (Fig. 5, *C* and *D*). Moreover, an accumulation of mutant $BrdU^+$ progenitors was detected in bins 9 and 10 corresponding to the intermediate zone (Fig. 5*D*). When labeled at E16.5, there was a decrease in bins 3–8 and 10 (Fig. 5, *E* and *F*). These results indicate that the lamination defects are evident as early as E14.5 and become more severe as the development progresses to E16.5.

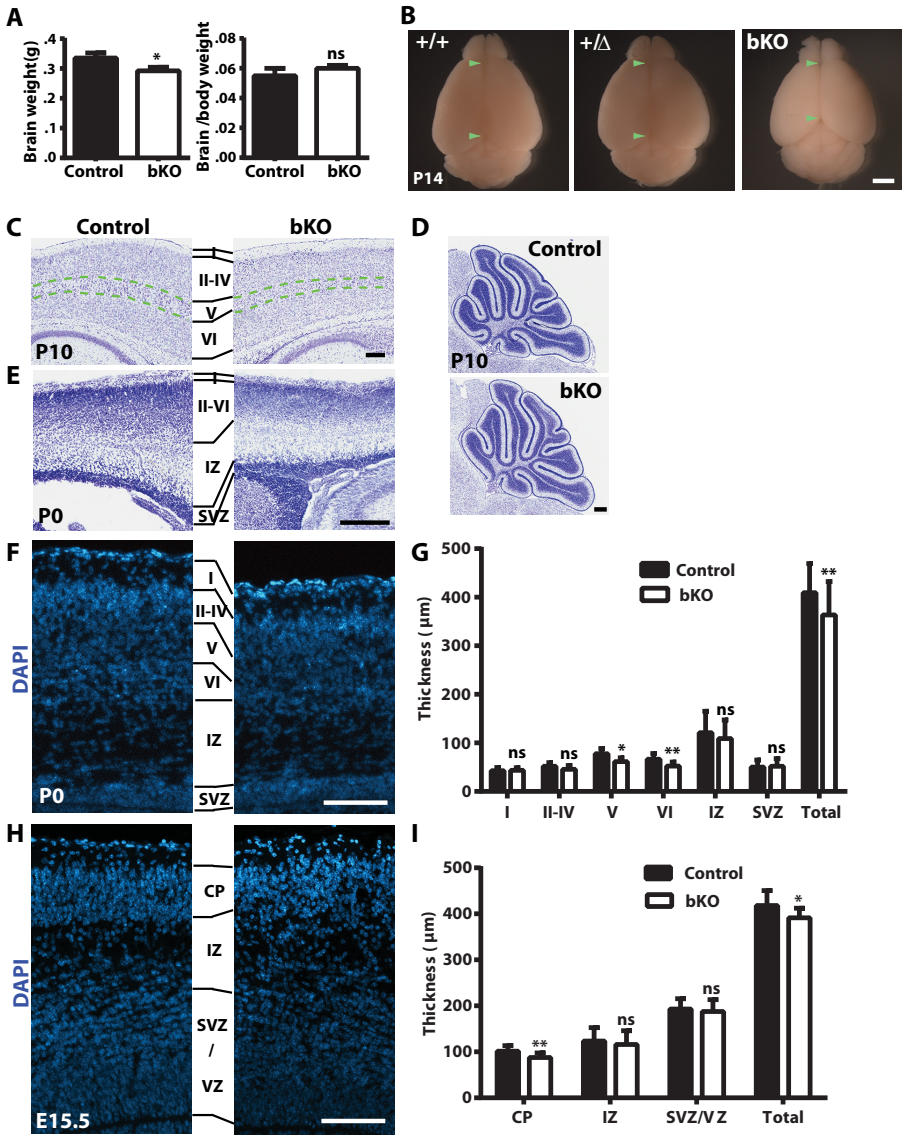

FIGURE 2. **Abnormal neocortex in the mutant brain.** *A,* decreased brain weight was observed in the bKO mice at P12, but the small brain size was proportional to decreased body weight ($n = 3$). *, $p < 0.05$; *ns*, not statistically significant. *B,* dorsal view of wild-type, heterozygous, and bKO brains at P14. Compared with the wild-type and heterozygote, the mutant brain displayed shorter rostral-caudal span (*flanked* with *green arrowheads*). *C–E,* Nissl staining of sagittal brain sections. At P10, the bKO mice had thinner cortex, especially layer V (*C*), although the mutant cerebellum was normal (*D*). The cortical difference was apparent at P0 (*E*). *F* and *G,* DAPI staining of brain sections at P0. Representative images are shown, and quantification of cortical layer thickness is presented. The entire cortex and layers V–VI were significantly thinner in the mutant. Data were based on images from three mice per genotype and 3–4 sections per mouse. *H* and *I,* DAPI staining of fetal brain sections at E15.5. The developing cortex in the mutant, notably in the cortical plate (*CP*), was thinner than that in the wild type. Data were from three fetuses per genotype and 4–5 sections per fetus. *Scale bars,* 2 mm for *B*; 200 μm for *C–E*; and 100 μm for *F* and *H*. *I-VI*, cortical layer I-VI; *CP,* cortical plate; *IZ,* intermediate zone; *SVZ,* subventricular zone; *VZ,* ventricular zone; *ns*, not statistically significant; *, $p < 0.05$, **, $p < 0.01$.

Neuronal progenitors are important for neocortical lamination (50, 52). Because we observed a thinner cortical plate in the mutant as early as E15.5 (Fig. 2*I*), we analyzed proliferation of ventricular and subventricular cortical progenitors by immunostaining for Ser-10-phosphorylated histone H3, a widely used marker of mitosis. The number of mitotic cells at the ventricular surface was significantly lower in the mutant (Fig. 6, *A* and *B*). To investigate how other phases of the cell cycle are affected, we carried out double labeling for BrdU and Ki67. For this, E15.5 pregnant mice were sacrificed after 1 h of BrdU labeling to retrieve fetal brains for immunofluorescence microscopy. Consistent with reduced mitotic cells in the ventricular surface (Fig. 6, *A* and *B*), total proliferating ($Ki67^+$) cells and the S phase ($BrdU^+Ki67^+$) cells declined significantly in the mutant subventricular zone (Fig. 6, *C–G*). However, the labeling index (*i.e.* the ratio of $BrdU^+Ki67^+$ *versus* $Ki67^+$ cells) remained unchanged in the mutant (Fig. 6*H*), indicating that neuronal progenitors cycle at similar rates of lamination (43, 60). This is very similar to what was reported for mice lacking the T-box transcription factor Tbr2 (43, 60). To assess whether the reduced cortical thickness is due to apoptosis, we performed immunostaining for activated caspase-3. No apoptotic signals were detected in the control or bKO fetal forebrain (data not shown). These results suggest that Brpf1 loss reduces the neuronal progenitor pool.

To substantiate this, we examined $Tbr2^+$ intermediate neuronal progenitors (or basal progenitors), which are known to be important for cortical lamination (43, 60). These progenitors

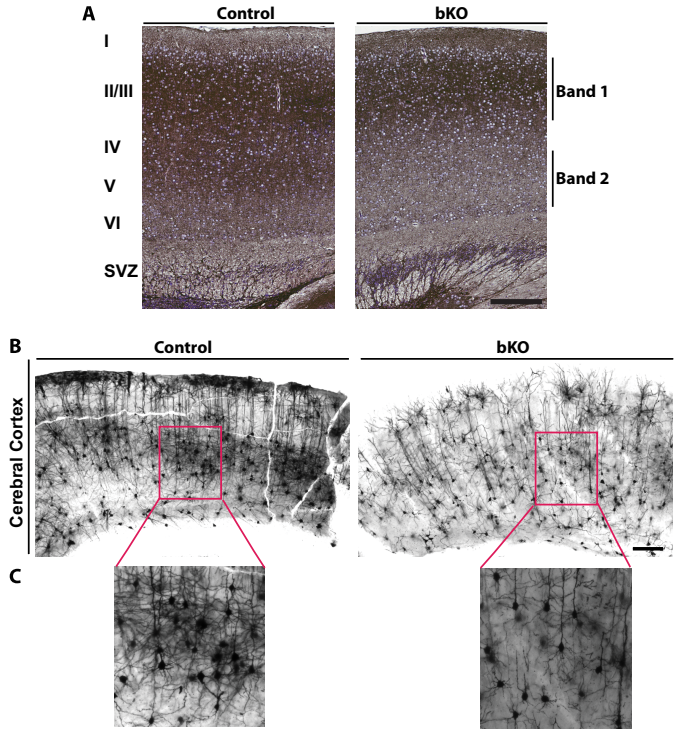

FIGURE 3. **Abnormal neuron organization in the mutant neocortex.** *A,* Timm's stain of brain sections at P8. Representative images of the neocortical region above the hippocampus were taken from stained wild-type and mutant sections. *I–VI* means neocortical layers I–VI. *B* and *C,* Golgi-Cox staining of brain sections at P19. Images of representative neocortical regions in control and bKO brain sections are shown in *B,* and high magnification images of regions *boxed* in *B* are presented in *C*. Compared with the control, the mutant cortex was less organized and contained fewer neurons. *Scale bars,* 250 μm for *A* and 200 μm for *B*.

decreased significantly in the subventricular zone of the mutant neonate cortex (Fig. 6, *I* and *J*). However, $Sox2^+$ neural stem cells were not affected (Fig. 6, *K* and *L*). These results support the idea that Brpf1 deficiency compromises neuronal progenitor production.

Brpf1 Loss Leads to Callosal Hypoplasia—In addition to the abnormal neocortex in the mutant brain, we noticed the absence of the corpus callosum in the ventral and dorsal but not the middle transverse sections at P14 (Fig. 7*A*), The defect was also present at later time points such as P24 (Fig. 8*A*) in the caudal part of serial coronal sections. To investigate whether the observed defects originate prior to birth, we analyzed wild-type and mutant brain sections at earlier developmental time points. As shown in Fig. 8*B*, the wild-type corpus callosum was similar to the mutant one at E17.5. However, the defect became evident caudally at P0 (Fig. 8*C*), indicating that the abnormality occurs shortly before birth. The corpus callosum contains axon tracks and is heavily myelinated, so we performed myelin staining. This staining confirmed partial callosal agenesis and also revealed defective myelination (Fig. 7*C*). Genitopatellar syndrome patients carrying MORF mutations display callosal agenesis (23, 24). Thus, the hypoplasia observed in Brpf1-deficient mice provide some insights into callosal agenesis in these patients.

Several groups of cells are crucial for callosal development, including the supracallosal gyrus (or indusium griseuem), which is located above the corpus callosum (61). Examination of Nissl-stained sections at high magnification revealed that the supracallosal gyrus was largely missing or ill-formed in the mutant (Fig. 7*B*). This provides a cellular mechanism whereby Brpf1 causes callosal agenesis. Molecularly, Tbr2 is important for callosal development, and its loss causes agenesis of the corpus callosum in human patients (62) and mice (60, 63). Related to this, Tbr2 expression decreased in the bKO brain (Fig. 6, *I* and *J*). Another transcription factor, Nr2f1, is also required for the formation of corpus callosum by regulating axonal growth in mice (64). Moreover, the axon guidance regulator roundabout 3 (Robo3) is important for midline axon crossing (65). As described in the section below, Nr2f1 and Robo3 transcript levels decreased in the mutant. These results indicate that Brpf1 loss reduces Tbr2, Nr2f1, and Robo3 expression, thereby leading to callosal hypoplasia.

Brpf1 Regulates Transcriptional Activation and Gene Silencing—To understand the underlying molecular mechanisms, we first analyzed transcripts of different layer markers, including Reelin, Rorβ, Fezf2, and Tbr1, which are known to govern the identity of layers I, IV, V, and VI, respectively (57). As shown in Fig. 9*A*, the knock-out efficiency was expected. Importantly, mRNA levels of layer IV–VI markers were reduced in bKO brains at both P10 and P24 (Fig. 9*B*). In addition to lamination, arealization is important for neocortical patterning (66, 67). Besides the layer V marker Fezf2, several other transcription factors, including Emx1, Pax6, and Nr2f1, are important for neocortical arealization. RT-PCR analysis revealed that their transcript levels were also altered at both P10 and P24 (Fig. 9*B*).

To investigate the impact on transcription systematically, we prepared total RNA from three pairs of control and mutant dorsal brain cortices at P4 for microarray-based gene expression analyses, leading to identification of ~200 genes with transcript levels reduced in the mutant by at least 3-fold. Among the top 50 are Robo3, osteocrin (also known as muslin), and the transcription factor Otx1 (Fig. 9*C* and supplemental Table S1). Robo3 controls neurite outgrowth (65), so its decreased expression is consistent with the defects observed in cortical neurogenesis (Figs. 4–6). Osteocrin is a novel peptide only known to be important for bone and muscle development (68), so its expression in the brain of young pups suggests a novel role in cortical development. Consistent with the observed cortical defects (Figs. 2–4), Otx1 is a marker of layer V pyramidal neurons, known to be composed of decreased Morf expression (27). RT-qPCR confirmed down-regulated expression of these three genes (Fig. 9*C* and supplemental Table S1). Gene Set Enrichment Analysis revealed ribosomal structural proteins as the top group whose expression was down-regulated in the mutant. RT-qPCR detected minimal changes in the levels of related transcripts (supplemental Table S1), indicating that expression of ribosomal structural proteins is not significantly affected.

Microarray analyses also uncovered ~100 genes whose transcript levels were elevated in the mutant by at least 3-fold. The top 40 exhibited elevation by >4-fold. Unexpectedly, among them are multiple *Hox* genes, including *Hoxa7, Hoxb5, Hoxb13, Hoxc4, Hoxc6, Hoxc10,* and *Hoxd8* (Fig. 9*C* and supplemental Table S1). Moreover, the elevation was dramatic as some of them (*e.g. Hoxb13, Hoxc4, Hoxc6,* and *HoxC10*) increased by

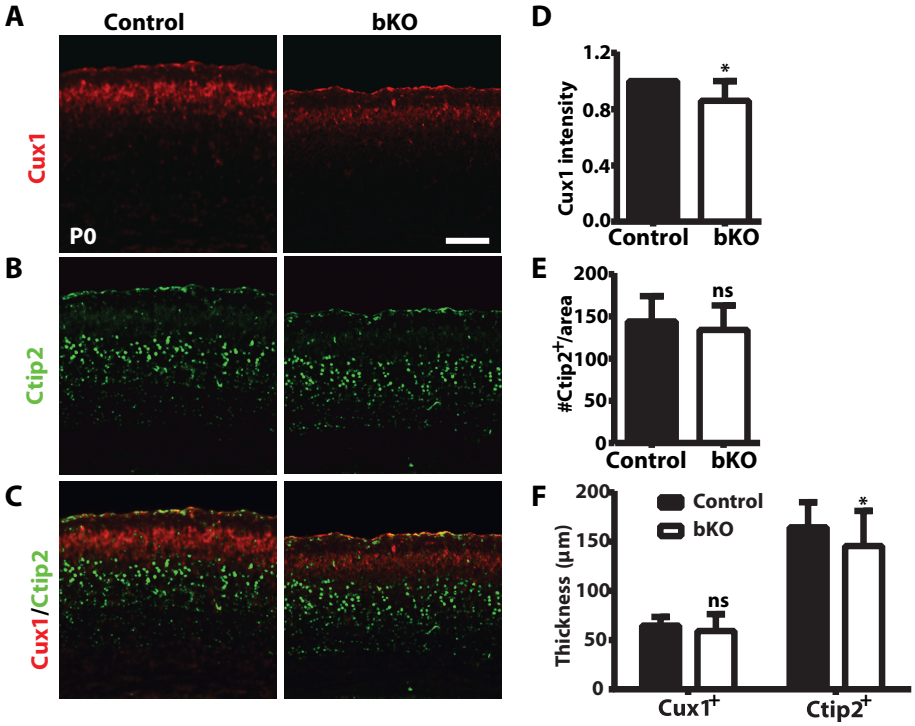

FIGURE 4. **Disorganization of Cux1$^+$ and Ctip2$^+$ layers in the mutant neocortex.** Brain sections were immunostained with anti-Cux1 (*red*) and -Ctip2 (*green*) antibodies at P0. Representative images are shown in *A–C* and quantification is presented in *D–F*. In the mutant, thickness of the Cux1$^+$ layer remained unchanged (*F*), but the Cux1 protein level (as indicated by fluorescence signal intensity) decreased (*D*). Compared with the control, there was no change in Ctip2$^+$ neuron density (*E*); the Ctip2$^+$ layer was thinner in the mutant (*F*). Quantification was based on three pairs of neonates and 3–4 sections per neonate. *Scale bar,* 100 μm. *ns*, not statistically significant; *, $p < 0.05$.

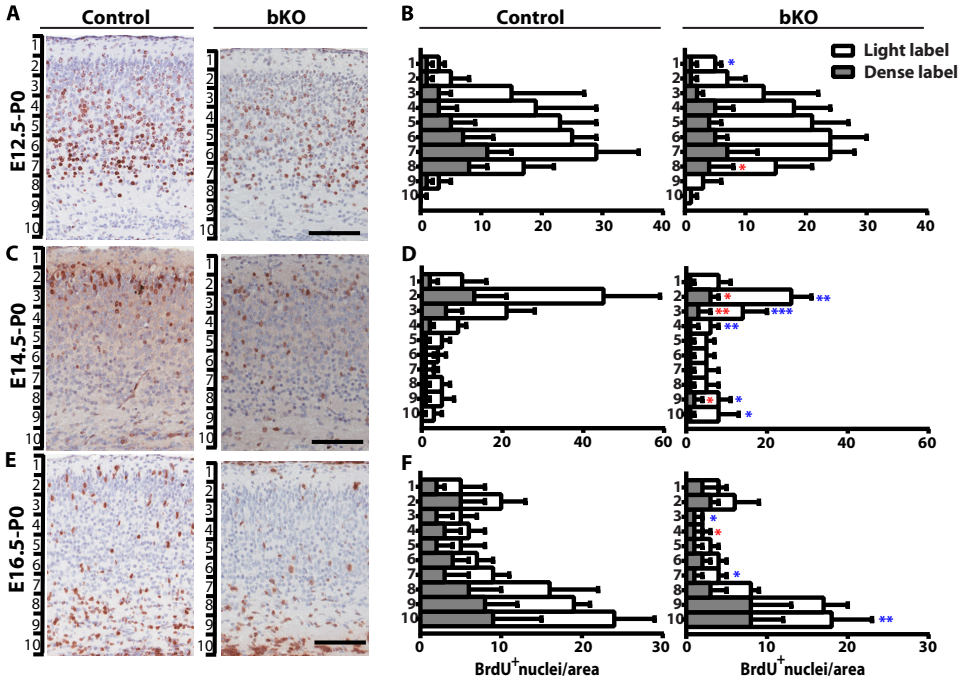

FIGURE 5. **Neuronal birthdating analysis.** After BrdU injection at E12.5, E14.5, and E16.5 into pregnant dams, control and mutant brains were collected at P0 for immunohistochemistry with anti-BrdU antibody. Representative images of the cortical region above the hippocampus are shown in *A*, *C*, and *E*, whereas the corresponding quantification results are presented as *bar graphs* in *B*, *D*, and *F*, respectively. As shown at the *left edge* of the images, each cortical section was divided into 10 evenly spaced bins, extending from the molecular layer to the intermediate zone, as reported previously (58, 59). Densely and lightly labeled BrdU$^+$ cells were then counted separately in each bin. Densely labeled cells are neurons that were born at the time of BrdU injection but had not experienced cell division by the time of analysis, whereas lightly labeled cells are the ones that had experienced cell division by the time of analysis. *Red* and *blue asterisks* denote statistical significance of densely and lightly labeled cells, respectively: *, $p < 0.05$; **, $p < 0.01$; ***, $p < 0.001$. The quantification was based on two pairs of control and mutant brains and at least four pairs of matched brain sections per pair of brains. *Scale bars,* 100 μm.

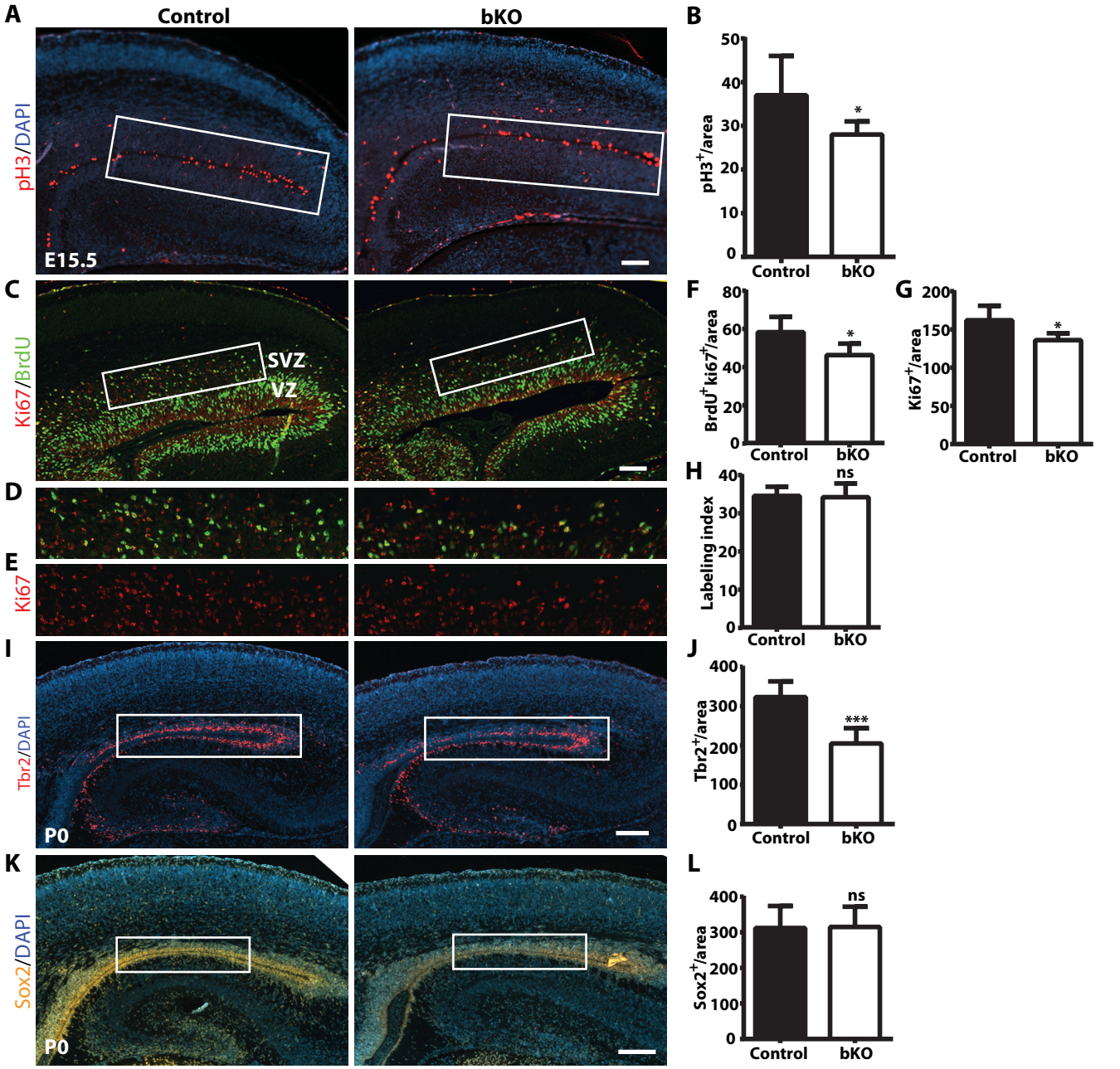

FIGURE 6. **Reduced neuronal progenitor pool in the mutant neocortex.** *A* and *B,* E15.5 fetal brain sections immunostained for Ser-10-phosphorylated histone H3. Representative images are shown in *A*, and the quantification in *B* is based on two fetuses per genotype and three sections per fetus. *C–E,* E15.5 fetal brain sections immunostained for Ki67 and BrdU. Fetuses were retrieved from pregnant dams after 1 h of labeling with BrdU. Merged and *red channel* images of the *boxed regions* in *C* are shown in *D* and *E*, respectively. *F–H,* quantification of the *boxed regions* in *C*, based on two fetuses per genotype and 4–5 sections per fetus. The labeling index refers to the ratio of $Ki67^+BrdU^+$ *versus* total $Ki67^+$ cells. *I* and *J,* reduced $Tbr2^+$ neuronal progenitors in the mutant ventricular surface at P0. Representative images are shown in *I* and the quantification, presented in *J*, was performed on three pairs of control and bKO brains and 3–4 sections per brain. *K* and *L*, number of $Sox2^+$ neural stem cells was minimally affected. Quantification was based on three pairs of control and bKO brains and three sections per brain. *, $p < 0.05$; *ns,* not statistically significant. *Scale bars,* 100 μm for *A* and *C*; 200 μm for *I* and *K*.

>100-fold (Fig. 9*C*). *Hox* genes are important for body patterning and hindbrain development, and they are normally silenced in the neocortex (69). Also among the top 40 are two other homeobox proteins, Hmx1 and En2 (Fig. 9*C* and supplemental Table S1). Hmx1 is important for development of craniofacial structures, and mutations in its gene cause oculoauricular syndrome with characteristics of defective eye and ear development (70). En2 is critical for cerebellar development, and its expression is a marker of prostate cancer (71). Other transcription factors among the top 40 are as follows: Lhx4 and Pitx2, crucial for pituitary gland development; Pou4f1, important for neurons in the brainstem and trigeminal ganglion; Foxa1, Onecut1, and Onecut2, controlling hepatic gene expression; Tbx5 and Pax1, regulating skeletogenesis in the limbs and ventral vertebral column, respectively; Nkx2–3, involved in inflammation response; and Twist1, important for craniofacial and limb development. Also among the top 40 is an uncharacterized cDNA clone, BC061194. The encoded protein is almost identi-

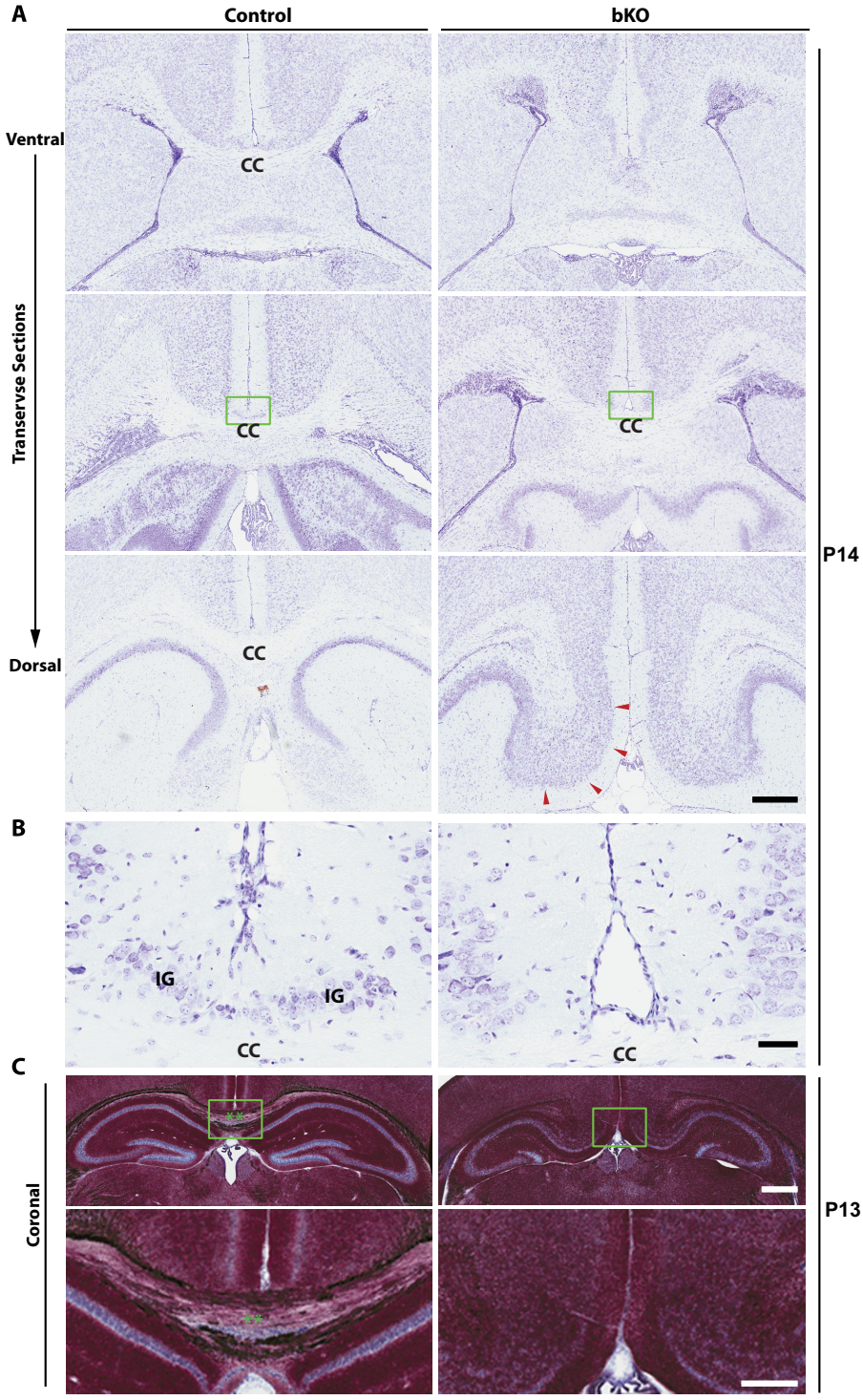

FIGURE 7. **Brpf1 loss causes defective callosal agenesis and abnormal myelination.** *A,* Nissl staining of transverse brain sections from control and bKO mice at P14. The corpus callosum (*CC*) was absent in the ventral and dorsal ends but present in the middle portion. Hyperplasia in the mutant subiculum is marked with *red arrowheads*. *B,* high magnification Nissl-stained image of the *boxed regions* in *A, middle panels*. *IG* stands for the indusium griseuem (also known as supracallosal gyrus), a group of cells key to formation of the corpus callosum. *C,* myelin staining was performed on coronal sections from P13 control and bKO brains, confirming callosal agenesis and revealing defective myelination in the mutant brain. *Scale bars,* 0.5 mm for *A*;50 μm for *B*; and 0.5 mm for the *upper panels* of *C* and 0.25 mm for the *lower panels*.

cal to that of the cytoskeletal protein Spag6, so we have referred to this new protein as Spag6l. RT-qPCR confirmed transcriptional up-regulation of the above transcription factors and Spag6l in the mutant (Fig. 9*C*). For example, by RT-qPCR, Hoxc4 mRNA increased in the mutant by >1000-fold (Fig. 9*C*). In agreement with this, the protein was not expressed in the heterozygotes (Fig. 9*D*, *lanes 1–3*) but became easily detectable in the mutant homozygotes (*lanes 4–6*). Normally, a majority of these genes are not expressed in the cerebral cortex, so the results from microarray analysis (supplemental Table S1), RT-

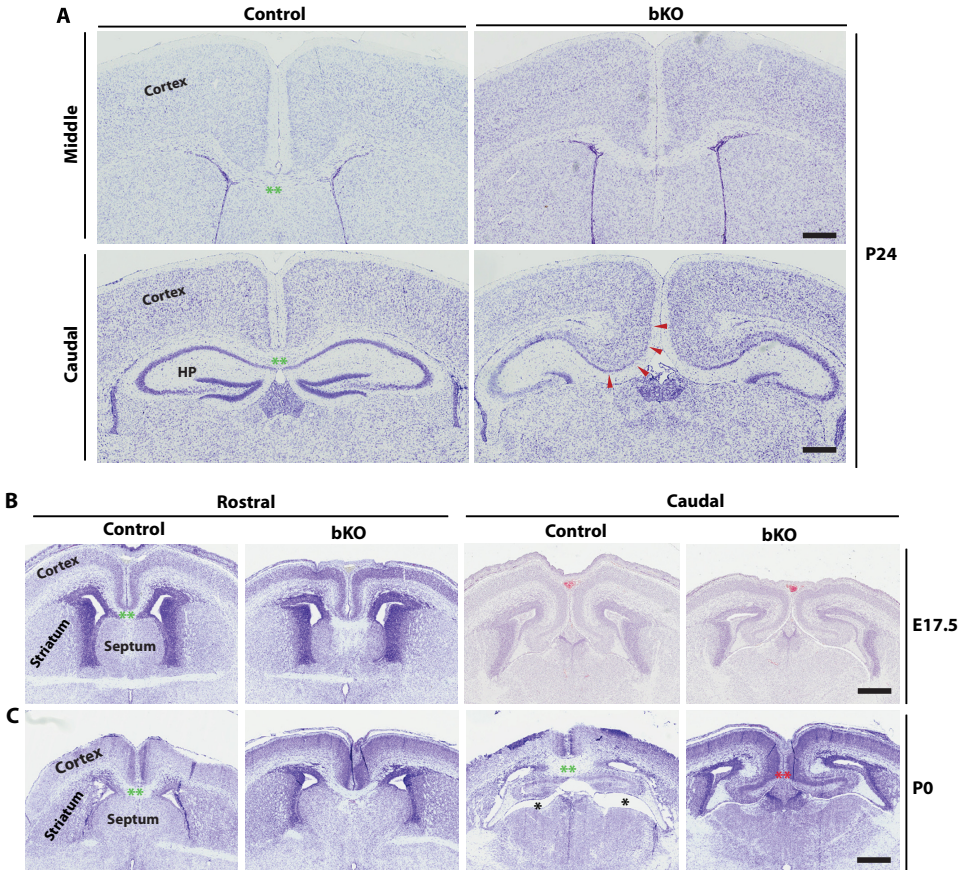

FIGURE 8. **Developmental origin of callosal agenesis.** *A,* Nissl staining was performed on serial coronal sections from control and bKO brains at P24. Two sets of representative images are shown here. The agenesis was evident at the caudal section of the mutant brain. Note hyperplasia in the subiculum (marked with *red arrowheads*) and hypoplasia in the dentate gyrus of the mutant hippocampus. *B* and *C,* Nissl staining was performed on serial coronal sections from control and bKO brains at E17.5 and P0. Two sets of representative images are shown. At E17.5, both control and bKO mice formed the rostral corpus callosum (marked by *green double asterisks*). At P0, the mutant corpus callosum failed to cross the midline caudally (*red double asterisks*). The *black asterisks* in *C* mark two regions accidentally torn during section processing. *Scale bars,* 0.5 mm.

qPCR (Fig. 9*C*), and immunoblotting (Fig. 9*D*) indicate that Brpf1 acts as a silencer to inhibit expression of these genes in the forebrain.

DISCUSSION

The human genome encodes hundreds of chromatin regulators. With many of them molecularly characterized, an emerging issue is how they control biological processes *in vivo*. This study identifies an important role of Brpf1, a unique chromatin regulator, in development of the neocortex and corpus callosum and regulating expression of *Hox* and other genes.

Brpf1 Regulates Forebrain Development—Forebrain-specific inactivation of the *Brpf1* gene caused early postnatal lethality (Fig. 1*A*), severe growth retardation (Fig. 1, *B* and *C*), and aberrant behaviors (Fig. 1, *D–H*). Histological analyses revealed disorganization of the neocortex (Figs. 2–4), abnormal neurogenesis (Figs. 5 and 6), and partial agenesis of the corpus callosum (Figs. 7 and 8). Although not characterized here, Brpf1 loss also led to hypoplasia of the dentate gyrus in the hippocampus (Fig. 8*A*).[3] Consistent with these results, Brpf1 is highly expressed in the neocortex and hippocampus (35). These novel findings support its important role in development of the mouse forebrain.

In addition to the forebrain, Brpf1 is highly expressed in the cerebellum (35), so it will be interesting to investigate whether Brpf1 plays a role in this structure. The $Brpf1^{f/+}$ line used herein should be valuable for this. Because the human *BRPF1* gene is mutated in sonic hedgehog-driven medulloblastoma (36), the role of mouse Brpf1 in the cerebellum is pathologically important. Its loss in the forebrain led to elevated expression of En2 and Twist1 (Fig. 9*C*), known to be important for tumorigenesis and metastasis. Whether such regulation also occurs in the cerebellum is an interesting question worth further investigation.

Molecularly, Brpf1 loss reduced the transcription of multiple genes important for lamination and arealization of the neocortex (Fig. 9, *A* and *B*). This role in transcriptional regulation is in agreement with published molecular and cell-based studies that Brpf1 and its partners, Moz and Morf, function as transcriptional co-activators (29). At the cellular level, Brpf1 loss altered distribution of cortical neurons (Figs. 4 and 5) and $Tbr2^{+}$ intermediate neuronal progenitors (Fig. 6, *I* and *J*). These progenitors are important not only for neocortical but also for callosal development (60, 72, 73). Moreover, TBR2 loss causes agenesis of the corpus callosum in humans and mice (60, 62, 63). Thus, deregulation of these progenitors provides a poten-

[3] You, L., Yan, K., Zou, J., Zhao, H., Bertos, N. R., Park, M., Wang, E., and Yang, X. J. (2015) The lysine acetyltransferase activator Brpf1 governs dentate gyrus development through neural progenitors and stem cells. *PLoS Genet.*, in press.

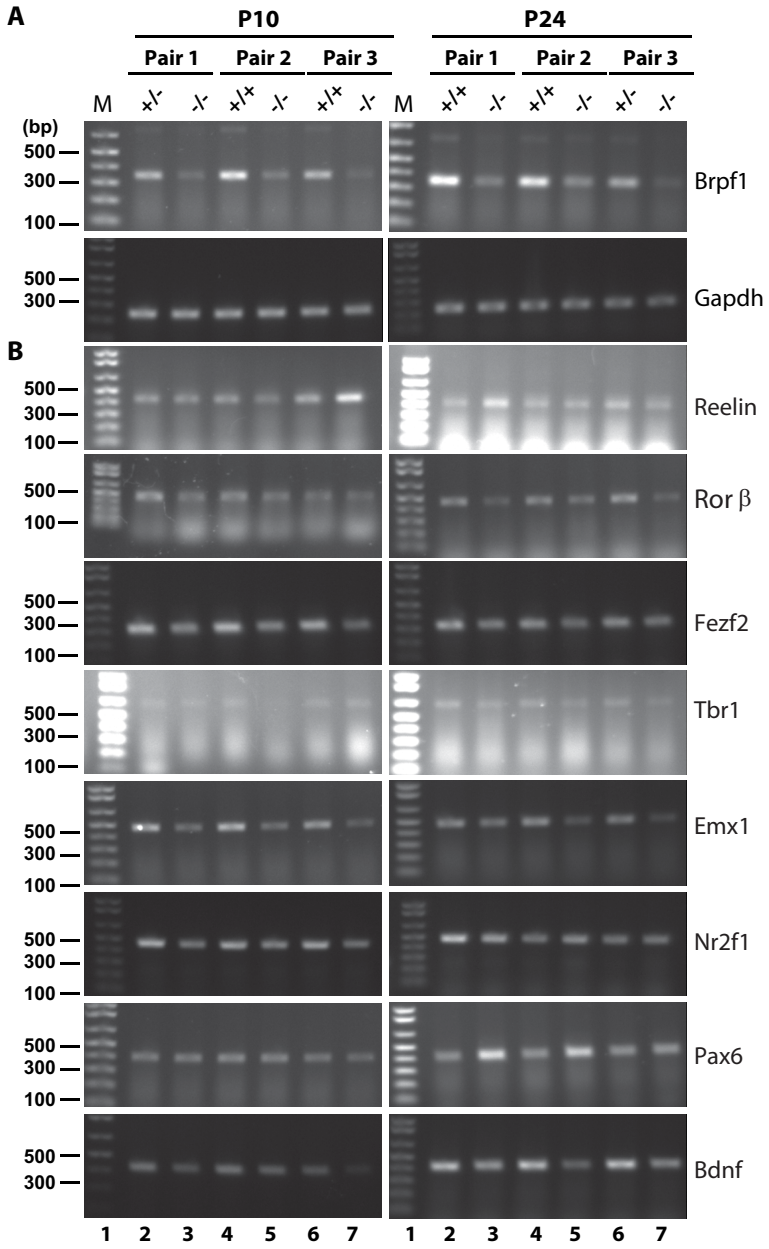

Gene	Microarray (fold)	RT-qPCR (fold)
Brpf1	0.5	0.3±0.3*
Robo3	0.4/0.3	0.3±0.1**
Ostn	0.1	0.2±0.1**
Hoxa7	6.0	?
Hoxb5	11.0	7.7±2.6*
Hoxb13	216.7	888.4±152.2***
Hoxc4	143.0	1455.5±367.6**
Hoxc6	224.4	505.0±172.1**
Hoxc10	3.0	1052.3±83.5***
Hoxd8	155.4	45.1±26.0*
Hmx1	7.2	168.7±45.4**
En2	6.0	11.2±1.6***
Lhx4	24.0/4.0	578.2±159.3**
Pitx2	11.1	15.8±5.3**
Pou4f1	5.2	20.1±5.3**
Foxa1	45.9	279.3±54.5***
Onecut1	18.9/1.9/0.9	14.0±2.8**
Onecut2	3.9	4.1±0.8**
Tbx5	22.3	183.9±31.9***
Pax1	17.5	88.1±8.1***
Nkx2-3	7.3	24.2±6.5**
Twist1	4.0	10.1±1.7***
Spag6l	16.3/6.5	3.3±0.6**

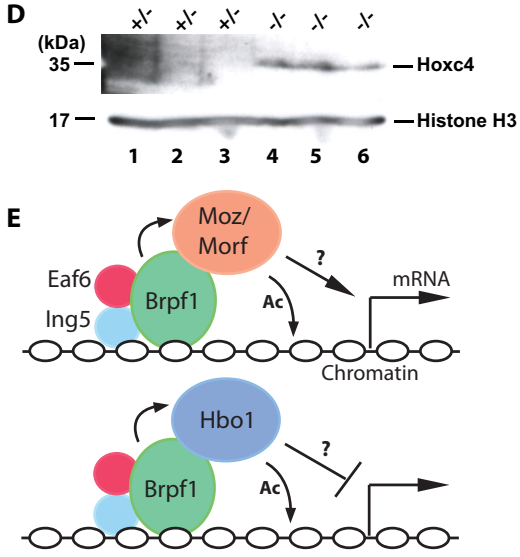

FIGURE 9. **Dual role of Brpf1 in regulating gene expression.** *A*, RT-PCR of dorsal caudal cortices to determine the knock-out efficiency. Gapdh was used as the internal control. *M*, 100-bp DNA ladder. $n = 3$ pairs for each of the 2 postnatal days, P10 and P24. *B*, same as *A* except cortical layer markers Reelin (layer I), Rorβ (layer IV), Fezf2 (layer V), and Tbr1 (layer VI) and four neurogenic factors (Emx1, Nr2f1, Pax6, and Bdnf) were analyzed. *C*, selected genes identified by microarray analysis of three pairs of control and bKO dorsal caudal cortices at P4. The fold values denote the mutant transcript levels divided by the control. Some genes have more than one value due to multiple probes used in the arrays. Validation was performed with RT-qPCR on three pairs of control and bKO dorsal caudal cortices at P12. *, $p < 0.05$; **, $p < 0.01$; ***, $p < 0.001$. *D*, immunoblotting for Hoxc4 in three pairs of heterozygous (*lanes 1–3*) and bKO (*lanes 4–6*) dorsal caudal cortices at P12. Histone H3 was used as the loading control. *E*, models illustrate that Brpf1 forms a trimeric complex with Ing5 and Eaf6 to recruit the histone acetyltransferases Moz/Morf and Hbo1 to regulate gene expression. *Question marks* denote that consequences of recruitment of Moz/Morf and Hbo1 remain unclear. *Ac*, acetylation.

tial mechanism whereby *Brpf1* inactivation led to cortical abnormalities (Figs. 2–6) and partial callosal agenesis (Figs. 7 and 8).

Brpf1 is paralogous to Brpf2 and Brpf3 (16). Loss of mouse Brpf2 leads to multiple defects in neural tube closure, eye development, and erythropoiesis (74), but it remains unclear what roles Brpf2 may play in the brain. Moreover, little is known about the biological functions of Brpf3. The defective development observed here indicates that Brpf1 has functions that neither Brpf2 nor Brpf3 can substitute. Thus, this study reiterates the notion that the three mammalian proteins have distinct roles *in vivo*.

Interaction of Brpf1 with Moz, Morf, and Hbo1 in the Brain—According to molecular and cell-based assays, Brpf1 interacts with the three acetyltransferases Moz, Morf, and Hbo1 to stimulate their enzymatic activities and control their substrate specificity (28–30), so an interesting question is how these enzymes may contribute to the defects caused by *Brpf1* inactivation (Fig. 9*E*). Mice with residual *Morf* expression display abnormalities in the neocortex (27). Importantly, mutations in the *MORF*

gene causes Noonan syndrome-like disorder (21), Ohdo syndrome (22), genitopatellar syndrome (23, 24), and blepharophimosis-ptosis-epicanthus inversus syndrome (25). Patients with these diseases display intellectual disability and ill-formed corpus callosum (26). Thus, the defective noecortex and corpus callosum in the Brpf1 mutant mice suggest that Morf may be an immediate target of Brpf1 in the mouse forebrain (Fig. 9*E*, *top panel*). However, it should be noted that both mouse Moz and Hbo1 are also expressed in the cerebral cortex and hippocampus (35), so it remains to be investigated whether and how these two acetyltransferases mediate Brpf1-dependent actions in the forebrain. Further studies are needed to dissect the relative contribution of these three acetyltransferases to the role of Brpf1 in regulating forebrain development (Fig. 9*E*). As discussed below, rather than the linear relationship that cell-based studies have suggested (28–30), Brpf1 may differentially interact with the acetyltransferases according to various developmental contexts.

Brpf1 Activates or Represses Transcription in a Context-dependent Manner—Interestingly, microarray-based gene expression analysis revealed that in addition to down-regulation of gene expression, Brpf1 loss dramatically up-regulated transcription of different *Hox* genes and the genes of multiple transcription factors important in various developmental processes (supplemental Table S1 and Fig. 9*C*). RT-qPCR and immunoblotting confirmed this (Fig. 9, *C* and *D*). Notably, no such up-regulation was detected in Brpf1-deficient embryos or mouse embryonic fibroblasts (data not shown), supporting that the repressive role of Brpf1 is specific to the brain. Normally, a majority of these genes is not expressed in the forebrain, so the results indicate that Brpf1 is required for silencing gene expression in brain development. This is striking and unexpected.

In stark contrast, fish Brpf1 is important for maintaining *Hox* gene expression during skeletal development (75, 76). Consistent with this, fish Moz is essential for *Hox* gene expression during skeletogenesis (77, 78). In agreement with these fish genetic studies, mouse Moz regulates segmental identity and *Hox* gene expression (79). Thus, both Brpf1 and Moz activate *Hox* gene expression during skeletal development in fish and mice. It is noteworthy, however, that little is known about the function of Moz in the brain. One study indicates that mouse Moz regulates neural stem cell proliferation by repressing p16 expression (80), but it remains unclear how this repression occurs.

Interestingly, related to the repressive role of Brpf1 in forebrain *Hox* gene expression (supplemental Table S1 and Fig. 9, *C* and *D*), the fly HBO1 ortholog Chameau is essential for *Hox* gene silencing by polycomb group proteins (31). Moreover, Chameau functionally replaces yeast Sas2 (something about silencing) *in vivo* (31). Sas2 was initially identified as a gene silencer and is a founding member of the MYST family of histone acetyltransferases (81). In light of their similar roles in silencing *Hox* gene expression, it is tempting to propose that Brpf1 interacts with Hbo1 and acts as a gene silencer in the forebrain (Fig. 9*E*, *bottom panel*). Further studies are needed to investigate this hypothesis and to determine the function of Hbo1 in the mouse brain.

In conclusion, Brpf1 plays an important role in development of the neocortex and corpus callosum by regulating related neurogenesis and transcriptional programs. Our results also suggest that depending on cellular and developmental contexts, Brpf1 functions either as an activator or a silencer of gene expression *in vivo*.

REFERENCES

1. Berger, S. L. (2007) The complex language of chromatin regulation during transcription. *Nature* **447,** 407–412
2. Kouzarides, T. (2007) Chromatin modifications and their function. *Cell* **128,** 693–705
3. Suganuma, T., and Workman, J. L. (2011) Signals and combinatorial functions of histone modifications. *Annu. Rev. Biochem.* **80,** 473–499
4. Dawson, M. A., and Kouzarides, T. (2012) Cancer epigenetics: from mechanism to therapy. *Cell* **150,** 12–27
5. You, J. S., and Jones, P. A. (2012) Cancer genetics and epigenetics: two sides of the same coin? *Cancer Cell* **22,** 9–20
6. Butler, J. S., and Dent, S. Y. (2013) The role of chromatin modifiers in normal and malignant hematopoiesis. *Blood* **121,** 3076–3084
7. Urdinguio, R. G., Sanchez-Mut, J. V., and Esteller, M. (2009) Epigenetic mechanisms in neurological diseases: genes, syndromes, and therapies. *Lancet Neurol.* **8,** 1056–1072
8. Jakovcevski, M., and Akbarian, S. (2012) Epigenetic mechanisms in neurological disease. *Nat. Med.* **18,** 1194–1204
9. Ronan, J. L., Wu, W., and Crabtree, G. R. (2013) From neural development to cognition: unexpected roles for chromatin. *Nat. Rev. Genet.* **14,** 347–359
10. Petrij, F., Giles, R. H., Dauwerse, H. G., Saris, J. J., Hennekam, R. C., Masuno, M., Tommerup, N., van Ommen, G. J., Goodman, R. H., and Peters, D. J. (1995) Rubinstein-Taybi syndrome caused by mutations in the transcriptional co-activator CBP. *Nature* **376,** 348–351
11. Roelfsema, J. H., White, S. J., Ariyürek, Y., Bartholdi, D., Niedrist, D., Papadia, F., Bacino, C. A., den Dunnen, J. T., van Ommen, G. J., Breuning, M. H., Hennekam, R. C., and Peters, D. J. (2005) Genetic heterogeneity in Rubinstein-Taybi syndrome: mutations in both the CBP and EP300 genes cause disease. *Am. J. Hum. Genet.* **76,** 572–580
12. Gräff, J., Rei, D., Guan, J. S., Wang, W. Y., Seo, J., Hennig, K. M., Nieland, T. J., Fass, D. M., Kao, P. F., Kahn, M., Su, S. C., Samiei, A., Joseph, N., Haggarty, S. J., Delalle, I., and Tsai, L. H. (2012) An epigenetic blockade of cognitive functions in the neurodegenerating brain. *Nature* **483,** 222–226
13. Williams, S. R., Aldred, M. A., Der Kaloustian, V. M., Halal, F., Gowans, G., McLeod, D. R., Zondag, S., Toriello, H. V., Magenis, R. E., and Elsea, S. H. (2010) Haploinsufficiency of HDAC4 causes brachydactyly mental retardation syndrome, with brachydactyly type E, developmental delays, and behavioral problems. *Am. J. Hum. Genet.* **87,** 219–228
14. Chesi, A., Staahl, B. T., Jovičić, A., Couthouis, J., Fasolino, M., Raphael, A. R., Yamazaki, T., Elias, L., Polak, M., Kelly, C., Williams, K. L., Fifita, J. A., Maragakis, N. J., Nicholson, G. A., King, O. D., Reed, R., Crabtree, G. R., Blair, I. P., Glass, J. D., and Gitler, A. D. (2013) Exome sequencing to identify *de novo* mutations in sporadic ALS trios. *Nat. Neurosci.* **16,** 851–855
15. Göttlicher, M., Minucci, S., Zhu, P., Krämer, O. H., Schimpf, A., Giavara, S., Sleeman, J. P., Lo Coco, F., Nervi, C., Pelicci, P. G., and Heinzel, T. (2001) Valproic acid defines a novel class of HDAC inhibitors inducing differentiation of transformed cells. *EMBO J.* **20,** 6969–6978
16. Yang, X. J., and Ullah, M. (2007) MOZ and MORF, two large MYSTic HATs in normal and cancer stem cells. *Oncogene* **26,** 5408–5419
17. Borrow, J., Stanton, V. P., Jr., Andresen, J. M., Becher, R., Behm, F. G., Chaganti, R. S., Civin, C. I., Disteche, C., Dubé, I., Frischauf, A. M., Horsman, D., Mitelman, F., Volinia, S., Watmore, A. E., and Housman, D. E. (1996) The translocation t(8;16)(p11;p13) of acute myeloid leukaemia fuses a putative acetyltransferase to the CREB-binding protein. *Nat. Genet.* **14,** 33–41
18. Champagne, N., Bertos, N. R., Pelletier, N., Wang, A. H., Vezmar, M., Yang, Y., Heng, H. H., and Yang, X. J. (1999) Identification of a human histone acetyltransferase related to monocytic leukemia zinc finger pro-

tein. *J. Biol. Chem.* **274,** 28528–28536
19. Wu, X., Northcott, P. A., Dubuc, A., Dupuy, A. J., Shih, D. J., Witt, H., Croul, S., Bouffet, E., Fults, D. W., Eberhart, C. G., *et al.* (2012) Clonal selection drives genetic divergence of metastatic medulloblastoma. *Nature* **482,** 529–533
20. Voss, A. K., Vanyai, H. K., Collin, C., Dixon, M. P., McLennan, T. J., Sheikh, B. N., Scambler, P., and Thomas, T. (2012) MOZ regulates the Tbx1 locus, and moz mutation partially phenocopies DiGeorge syndrome. *Dev. Cell* **23,** 652–663
21. Kraft, M., Cirstea, I. C., Voss, A. K., Thomas, T., Goehring, I., Sheikh, B. N., Gordon, L., Scott, H., Smyth, G. K., Ahmadian, M. R., *et al.* (2011) Disruption of the histone acetyltransferase MYST4 leads to a Noonan syndrome-like phenotype and hyperactivated MAPK signaling in humans and mice. *J. Clin. Invest.* **121,** 3479–3491
22. Clayton-Smith, J., O'Sullivan, J., Daly, S., Bhaskar, S., Day, R., Anderson, B., Voss, A. K., Thomas, T., Biesecker, L. G., Smith, P., *et al.* (2011) Whole-exome-sequencing identifies mutations in histone acetyltransferase gene KAT6B in individuals with the Say-Barber-Biesecker variant of Ohdo syndrome. *Am. J. Hum. Genet.* **89,** 675–681
23. Simpson, M. A., Deshpande, C., Dafou, D., Vissers, L. E., Woollard, W. J., Holder, S. E., Gillessen-Kaesbach, G., Derks, R., White, S. M., Cohen-Snuijf, R., *et al.* (2012) *De novo* mutations of the gene encoding the histone acetyltransferase KAT6B cause genitopatellar syndrome. *Am. J. Hum. Genet.* **90,** 290–294
24. Campeau, P. M., Kim, J. C., Lu, J. T., Schwartzentruber, J. A., Abdul-Rahman, O. A., Schlaubitz, S., Murdock, D. M., Jiang, M. M., Lammer, E. J., Enns, G. M., *et al.* (2012) Mutations in KAT6B, encoding a histone acetyltransferase, cause genitopatellar syndrome. *Am. J. Hum. Genet.* **90,** 282–289
25. Yu, H. C., Geiger, E. A., Medne, L., Zackai, E. H., and Shaikh, T. H. (2014) An individual with blepharophimosis-ptosis-epicanthus inversus syndrome (BPES) and additional features expands the phenotype associated with mutations in KAT6B. *Am. J. Med. Genet. A* **164,** 950–957
26. Campeau, P. M., Lu, J. T., Dawson, B. C., Fokkema, I. F., Robertson, S. P., Gibbs, R. A., and Lee, B. H. (2012) The KAT6B-related disorders genitopatellar syndrome and Ohdo/SBBYS syndrome have distinct clinical features reflecting distinct molecular mechanisms. *Hum. Mutat.* **33,** 1520–1525
27. Thomas, T., Voss, A. K., Chowdhury, K., and Gruss, P. (2000) Querkopf, a MYST family histone acetyltransferase, is required for normal cerebral cortex development. *Development* **127,** 2537–2548
28. Doyon, Y., Cayrou, C., Ullah, M., Landry, A. J., Côté, V., Selleck, W., Lane, W. S., Tan, S., Yang, X. J., and Côté, J. (2006) ING tumor suppressors are critical regulators of chromatin acetylation required for genome expression and perpetuation. *Mol. Cell* **21,** 51–64
29. Ullah, M., Pelletier, N., Xiao, L., Zhao, S. P., Wang, K., Degerny, C., Tahmasebi, S., Cayrou, C., Doyon, Y., Goh, S. L., *et al.* (2008) Molecular architecture of quartet MOZ/MORF histone acetyltransferase complexes. *Mol. Cell. Biol.* **28,** 6828–6843
30. Lalonde, M. E., Avvakumov, N., Glass, K. C., Joncas, F. H., Saksouk, N., Paquet, E., Yan, K., Holliday, M., Tan, S., Yang, X. J., *et al.* (2013) Exchange of associated factors directs a switch in HBO1 acetyltransferase histone tail specificity. *Genes Dev.* **27,** 2009–2024
31. Grienenberger, A., Miotto, B., Sagnier, T., Cavalli, G., Schramke, V., Geli, V., Mariol, M. C., Berenger, H., Graba, Y., and Pradel, J. (2002) The MYST domain acetyltransferase Chameau functions in epigenetic mechanisms of transcriptional repression. *Curr. Biol.* **12,** 762–766
32. Lubula, M. Y., Eckenroth, B. E., Carlson, S., Poplawski, A., Chruszcz, M., and Glass, K. C. (2014) Structural insights into recognition of acetylated histone ligands by the BRPF1 bromodomain. *FEBS Lett.* **588,** 3844–3854
33. Vezzoli, A., Bonadies, N., Allen, M. D., Freund, S. M., Santiveri, C. M., Kvinlaug, B. T., Huntly, B. J., Göttgens, B., and Bycroft, M. (2010) Molecular basis of histone H3K36me3 recognition by the PWWP domain of Brpf1. *Nat. Struct. Mol. Biol.* **17,** 617–619
34. Wu, H., Zeng, H., Lam, R., Tempel, W., Amaya, M. F., Xu, C., Dombrovski, L., Qiu, W., Wang, Y., and Min, J. (2011) Structural and histone binding ability characterizations of human PWWP domains. *PLoS One* **6,** e18919
35. You, L., Chen, L., Penney, J., Miao, D., and Yang, X. J. (2014) Expression atlas of the epigenetic regulator Brpf1 and its requirement for survival of mouse embryos. *Epigenetics* **9,** 860–872
36. Kool, M., Jones, D. T., Jäger, N., Northcott, P. A., Pugh, T. J., Hovestadt, V., Piro, R. M., Esparza, L. A., Markant, S. L., Remke, M., *et al.* (2014) Genome sequencing of SHH medulloblastoma predicts genotype-related response to smoothened inhibition. *Cancer Cell* **25,** 393–405
37. Deacon, R. M. (2006) Assessing nest building in mice. *Nat. Protoc.* **1,** 1117–1119
38. Deacon, R. (2012) Assessing burrowing, nest construction, and hoarding in mice. *J. Vis. Exp.* **59,** e2607
39. Yamamoto, A., Lucas, J. J., and Hen, R. (2000) Reversal of neuropathology and motor dysfunction in a conditional model of Huntington's disease. *Cell* **101,** 57–66
40. Kim, G. W., Li, L., Gorbani, M., You, L., and Yang, X. J. (2013) Mice lacking α-tubulin acetyltransferase 1 are viable but display α-tubulin acetylation deficiency and dentate gyrus distortion. *J. Biol. Chem.* **288,** 20334–20350
41. Walkinshaw, D. R., Weist, R., Kim, G. W., You, L., Xiao, L., Nie, J., Li, C. S., Zhao, S., Xu, M., and Yang, X. J. (2013) The tumor suppressor kinase LKB1 activates the downstream kinases SIK2 and SIK3 to stimulate nuclear export of class IIa histone deacetylases. *J. Biol. Chem.* **288,** 9345–9362
42. Sansregret, L., Vadnais, C., Livingstone, J., Kwiatkowski, N., Awan, A., Cadieux, C., Leduy, L., Hallett, M. T., and Nepveu, A. (2011) Cut homeobox 1 causes chromosomal instability by promoting bipolar division after cytokinesis failure. *Proc. Natl. Acad. Sci. U.S.A.* **108,** 1949–1954
43. Arnold, S. J., Huang, G. J., Cheung, A. F., Era, T., Nishikawa, S., Bikoff, E. K., Molnár, Z., Robertson, E. J., and Groszer, M. (2008) The T-box transcription factor Eomes/Tbr2 regulates neurogenesis in the cortical subventricular zone. *Genes Dev.* **22,** 2479–2484
44. Mairet-Coello, G., Tury, A., Van Buskirk, E., Robinson, K., Genestine, M., and DiCicco-Bloom, E. (2012) p57(KIP2) regulates radial glia and intermediate precursor cell cycle dynamics and lower layer neurogenesis in developing cerebral cortex. *Development* **139,** 475–487
45. Cubelos, B., Sebastián-Serrano, A., Kim, S., Moreno-Ortiz, C., Redondo, J. M., Walsh, C. A., and Nieto, M. (2008) Cux-2 controls the proliferation of neuronal intermediate precursors of the cortical subventricular zone. *Cereb. Cortex* **18,** 1758–1770
46. Li, J., Lenferink, A. E., Deng, Y., Collins, C., Cui, Q., Purisima, E. O., O'Connor-McCourt, M. D., and Wang, E. (2010) Identification of high-quality cancer prognostic markers and metastasis network modules. *Nat. Commun.* **1,** 34
47. Gorski, J. A., Talley, T., Qiu, M., Puelles, L., Rubenstein, J. L., and Jones, K. R. (2002) Cortical excitatory neurons and glia, but not GABAergic neurons, are produced in the Emx1-expressing lineage. *J. Neurosci.* **22,** 6309–6314
48. Mangiarini, L., Sathasivam, K., Seller, M., Cozens, B., Harper, A., Hetherington, C., Lawton, M., Trottier, Y., Lehrach, H., Davies, S. W., and Bates, G. P. (1996) Exon 1 of the HD gene with an expanded CAG repeat is sufficient to cause a progressive neurological phenotype in transgenic mice. *Cell* **87,** 493–506
49. Deacon, R. M. (2006) Digging and marble burying in mice: simple methods for *in vivo* identification of biological impacts. *Nat. Protoc.* **1,** 122–124
50. Bystron, I., Blakemore, C., and Rakic, P. (2008) Development of the human cerebral cortex: Boulder Committee revisited. *Nat. Rev. Neurosci.* **9,** 110–122
51. Bareyre, F. M., Kerschensteiner, M., Misgeld, T., and Sanes, J. R. (2005) Transgenic labeling of the corticospinal tract for monitoring axonal responses to spinal cord injury. *Nat. Med.* **11,** 1355–1360
52. López-Bendito, G., and Molnár, Z. (2003) Thalamocortical development: how are we going to get there? *Nat. Rev. Neurosci.* **4,** 276–289
53. Schuurmans, C., Armant, O., Nieto, M., Stenman, J. M., Britz, O., Klenin, N., Brown, C., Langevin, L. M., Seibt, J., Tang, H., *et al.* (2004) Sequential phases of cortical specification involve neurogenin-dependent and -independent pathways. *EMBO J.* **23,** 2892–2902
54. Palmiter, R. D., Cole, T. B., Quaife, C. J., and Findley, S. D. (1996) ZnT-3, a putative transporter of zinc into synaptic vesicles. *Proc. Natl. Acad. Sci. U.S.A.* **93,** 14934–14939
55. Das, G., Reuhl, K., and Zhou, R. (2013) The Golgi-Cox method. *Methods Mol. Biol.* **1018,** 313–321

56. Nepveu, A. (2001) Role of the multifunctional CDP/Cut/Cux homeodomain transcription factor in regulating differentiation, cell growth and development. *Gene* **270,** 1–15
57. Molyneaux, B. J., Arlotta, P., Menezes, J. R., and Macklis, J. D. (2007) Neuronal subtype specification in the cerebral cortex. *Nat. Rev. Neurosci.* **8,** 427–437
58. Sugitani, Y., Nakai, S., Minowa, O., Nishi, M., Jishage, K., Kawano, H., Mori, K., Ogawa, M., and Noda, T. (2002) Brn-1 and Brn-2 share crucial roles in the production and positioning of mouse neocortical neurons. *Genes Dev.* **16,** 1760–1765
59. Keays, D. A., Tian, G., Poirier, K., Huang, G. J., Siebold, C., Cleak, J., Oliver, P. L., Fray, M., Harvey, R. J., Molnár, Z., *et al.* (2007) Mutations in α-tubulin cause abnormal neuronal migration in mice and lissencephaly in humans. *Cell* **128,** 45–57
60. Sessa, A., Mao, C. A., Hadjantonakis, A. K., Klein, W. H., and Broccoli, V. (2008) Tbr2 directs conversion of radial glia into basal precursors and guides neuronal amplification by indirect neurogenesis in the developing neocortex. *Neuron* **60,** 56–69
61. Donahoo, A. L., and Richards, L. J. (2009) Understanding the mechanisms of callosal development through the use of transgenic mouse models. *Semin. Pediatr. Neurol.* **16,** 127–142
62. Baala, L., Briault, S., Etchevers, H. C., Laumonnier, F., Natiq, A., Amiel, J., Boddaert, N., Picard, C., Sbiti, A., Asermouh, A., *et al.* (2007) Homozygous silencing of T-box transcription factor EOMES leads to microcephaly with polymicrogyria and corpus callosum agenesis. *Nat. Genet.* **39,** 454–456
63. Choe, Y., Siegenthaler, J. A., and Pleasure, S. J. (2012) A cascade of morphogenic signaling initiated by the meninges controls corpus callosum formation. *Neuron* **73,** 698–712
64. Armentano, M., Filosa, A., Andolfi, G., and Studer, M. (2006) COUP-TFI is required for the formation of commissural projections in the forebrain by regulating axonal growth. *Development* **133,** 4151–4162
65. Jen, J. C., Chan, W. M., Bosley, T. M., Wan, J., Carr, J. R., Rüb, U., Shattuck, D., Salamon, G., Kudo, L. C., Ou, J., *et al.* (2004) Mutations in a human ROBO gene disrupt hindbrain axon pathway crossing and morphogenesis. *Science* **304,** 1509–1513
66. Bishop, K. M., Goudreau, G., and O'Leary, D. D. (2000) Regulation of area identity in the mammalian neocortex by Emx2 and Pax6. *Science* **288,** 344–349
67. O'Leary, D. D., Chou, S. J., and Sahara, S. (2007) Area patterning of the mammalian cortex. *Neuron* **56,** 252–269
68. Moffatt, P., and Thomas, G. P. (2009) Osteocrin–beyond just another bone protein? *Cell. Mol. Life Sci.* **66,** 1135–1139
69. Maden, M. (1998) Vertebrate development: a nervous vitamin. *Curr. Biol.* **8,** R846–R849
70. Munroe, R. J., Prabhu, V., Acland, G. M., Johnson, K. R., Harris, B. S., O'Brien, T. P., Welsh, I. C., Noden, D. M., and Schimenti, J. C. (2009) Mouse H6 Homeobox 1 (Hmx1) mutations cause cranial abnormalities and reduced body mass. *BMC Dev. Biol.* **9,** 27
71. Marszałł, M. P., Sroka, W., Adamowski, M., Słupski, P., Jarzemski, P., Siódmiak, J., and Odrowąż-Sypniewska, G. (2015) Engrailed-2 protein as a potential urinary prostate cancer biomarker: a comparison study before and after digital rectal examination. *Eur. J. Cancer Prev.* **24,** 51–56
72. Englund, C., Fink, A., Lau, C., Pham, D., Daza, R. A., Bulfone, A., Kowalczyk, T., and Hevner, R. F. (2005) Pax6, Tbr2, and Tbr1 are expressed sequentially by radial glia, intermediate progenitor cells, and postmitotic neurons in developing neocortex. *J. Neurosci.* **25,** 247–251
73. Farkas, L. M., Haffner, C., Giger, T., Khaitovich, P., Nowick, K., Birchmeier, C., Pääbo, S., and Huttner, W. B. (2008) Insulinoma-associated 1 has a pan-neurogenic role and promotes the generation and expansion of basal progenitors in the developing mouse neocortex. *Neuron* **60,** 40–55
74. Mishima, Y., Miyagi, S., Saraya, A., Negishi, M., Endoh, M., Endo, T. A., Toyoda, T., Shinga, J., Katsumoto, T., Chiba, T., *et al.* (2011) The Hbo1-Brd1/Brpf2 complex is responsible for global acetylation of H3K14 and required for fetal liver erythropoiesis. *Blood* **118,** 2443–2453
75. Hibiya, K., Katsumoto, T., Kondo, T., Kitabayashi, I., and Kudo, A. (2009) Brpf1, a subunit of the MOZ histone acetyl transferase complex, maintains expression of anterior and posterior Hox genes for proper patterning of craniofacial and caudal skeletons. *Dev. Biol.* **329,** 176–190
76. Laue, K., Daujat, S., Crump, J. G., Plaster, N., Roehl, H. H., Tübingen 2000 Screen Consortium, Kimmel, C. B., Schneider, R., and Hammerschmidt, M. (2008) The multidomain protein Brpf1 binds histones and is required for Hox gene expression and segmental identity. *Development* **135,** 1935–1946
77. Crump, J. G., Swartz, M. E., Eberhart, J. K., and Kimmel, C. B. (2006) Moz-dependent Hox expression controls segment-specific fate maps of skeletal precursors in the face. *Development* **133,** 2661–2669
78. Miller, C. T., Maves, L., and Kimmel, C. B. (2004) moz regulates Hox expression and pharyngeal segmental identity in zebrafish. *Development* **131,** 2443–2461
79. Voss, A. K., Collin, C., Dixon, M. P., and Thomas, T. (2009) Moz and retinoic acid coordinately regulate H3K9 acetylation, Hox gene expression, and segment identity. *Dev. Cell* **17,** 674–686
80. Perez-Campo, F. M., Costa, G., Lie-A-Ling, M., Stifani, S., Kouskoff, V., and Lacaud, G. (2014) MOZ-mediated repression of p16(INK) (4) (a) is critical for the self-renewal of neural and hematopoietic stem cells. *Stem Cells* **32,** 1591–1601
81. Reifsnyder, C., Lowell, J., Clarke, A., and Pillus, L. (1996) Yeast SAS silencing genes and human genes associated with AML and HIV-1 Tat interactions are homologous with acetyltransferases. *Nat. Genet.* **14,** 42–49